August 2016

The SLUGGS survey: the mass distribution in early-type galaxies within five effective radii and beyond

Adebusola Alabi
Swinburne University of Technology

Duncan Forbes
Swinburne University of Technology

Aaron Romanowsky
San Jose State University, aaron.romanowsky@sjsu.edu

Jean Brodie
University of California Observatories

Jay Strader
Michigan State University

See next page for additional authors

Recommended Citation

Adebusola Alabi, Duncan Forbes, Aaron Romanowsky, Jean Brodie, Jay Strader, Joachim Janz, Vincenzo Pota, Nicola Pastorello, Christopher Usher, Lee Spitler, Caroline Foster, Zachary Jennings, Alexa Villaume, and Sreeja Kartha. "The SLUGGS survey: the mass distribution in early-type galaxies within five effective radii and beyond" *Monthly Notices of the Royal Astronomical Society* (2016): 3838-3860. https://doi.org/10.1093/mnras/stw1213

Monthly Notices
of the
ROYAL ASTRONOMICAL SOCIETY

MNRAS **460,** 3838–3860 (2016)
Advance Access publication 2016 May 20

doi:10.1093/mnras/stw1213

The SLUGGS survey: the mass distribution in early-type galaxies within five effective radii and beyond

Adebusola B. Alabi,[1★] Duncan A. Forbes,[1] Aaron J. Romanowsky,[2,3] Jean P. Brodie,[3] Jay Strader,[4] Joachim Janz,[1] Vincenzo Pota,[5] Nicola Pastorello,[1] Christopher Usher,[1,6] Lee R. Spitler,[7,8] Caroline Foster,[7] Zachary G. Jennings,[3] Alexa Villaume[3] and Sreeja Kartha[1]

[1]*Centre for Astrophysics and Supercomputing, Swinburne University, Hawthorn, VIC 3122, Australia*
[2]*Department of Physics and Astronomy, San José State University, San Jose, CA 95192, USA*
[3]*University of California Observatories, 1156 High Street, Santa Cruz, CA 95064, USA*
[4]*Department of Physics and Astronomy, Michigan State University, East Lansing, MI 48824, USA*
[5]*INAF – Observatorio Astronomico di Capodimonte, Salita Moiariello, 16, I-80131 Napoli, Italy*
[6]*Astrophysics Research Institute, Liverpool John Moores University, Liverpool L3 5RF, UK*
[7]*Australian Astronomical Observatory, PO Box 915, North Ryde, NSW 1670, Australia*
[8]*Department of Physics and Astronomy, Macquarie University, North Ryde, NSW 2109, Australia*

Accepted 2016 May 18. Received 2016 May 18; in original form 2016 January 18

ABSTRACT

We study mass distributions within and beyond 5 effective radii (R_e) in 23 early-type galaxies from the SAGES Legacy Unifying Globulars and Galaxies Survey, using their globular cluster (GC) kinematic data. The data are obtained with Keck/DEep Imaging Multi-Object Spectrograph, and consist of line-of-sight velocities for ∼3500 GCs, measured with a high precision of ∼15 km s^{-1} per GC and extending out to ∼13 R_e. We obtain the mass distribution in each galaxy using the tracer mass estimator of Watkins et al. and account for kinematic substructures, rotation of the GC systems and galaxy flattening in our mass estimates. The observed scatter between our mass estimates and results from the literature is less than 0.2 dex. The dark matter fraction within 5 R_e (f_{DM}) increases from ∼0.6 to ∼0.8 for low- and high-mass galaxies, respectively, with some intermediate-mass galaxies (M_*∼10^{11} M$_\odot$) having low f_{DM} ∼ 0.3, which appears at odds with predictions from simple galaxy models. We show that these results are independent of the adopted orbital anisotropy, stellar mass-to-light (M/L) ratio, and the assumed slope of the gravitational potential. However, the low f_{DM} in the ∼10^{11} M$_\odot$ galaxies agrees with the cosmological simulations of Wu et al. where the pristine dark matter distribution has been modified by baryons during the galaxy assembly process. We find hints that these M_*∼10^{11} M$_\odot$ galaxies with low f_{DM} have very diffuse dark matter haloes, implying that they assembled late. Beyond 5 R_e, the M/L gradients are steeper in the more massive galaxies and shallower in both low and intermediate mass galaxies.

Key words: globular clusters: general – galaxies: evolution – galaxies: kinematics and dynamics.

1 INTRODUCTION

One of the fundamental properties of galaxies is their total mass (baryonic + dark matter). The total mass profiles of giant galaxies are dominated by baryons in the central parts, with the dark matter (DM) component becoming more dominant at large radii, eventually dominating the total mass budget. Studying the distribution of these mass components provides a viable way of testing galaxy formation and evolution models. For example, at the same stellar mass, early-type galaxies (ETGs) are thought to have a higher DM concentration compared to spiral galaxies. This is because the central portions of the haloes in ETGs are already in place at a higher redshift compared to spiral galaxies for the same galaxy mass (e.g. Thomas et al. 2009).

For late-type galaxies, it is relatively easy to determine the total mass distribution out to large radii using the motions of the readily available H I gas as a tracer of the galaxy potential. However, this exercise is more difficult for (individual) ETGs. This is because ETGs are generally poor in cold gas, their stellar motions are predominantly random by nature and at large galactocentric radii,

★E-mail: aalabi@swin.edu.au

they are optically faint. These properties combine to make studies of the mass distribution in ETGs challenging. Yet, to properly understand the DM content in ETGs, one needs to probe out to at least five effective radii (R_e), where DM is expected to begin dominating the enclosed mass (Romanowsky et al. 2003; Napolitano et al. 2005; Cappellari et al. 2015).

Various mass tracers such as planetary nebulae (PNe; e.g. Morganti et al. 2013), globular clusters (GCs; e.g. Pota et al. 2015) and diffuse X-ray gas (e.g. Su et al. 2014) have been used to explore the mass distribution in ETGs out to large radii. For PNe- and GC-based studies, their orbital distributions are usually not known, and are notoriously difficult to determine due to the mass–anisotropy degeneracy (Binney & Mamon 1982). The discrete kinematic data are often binned and smoothed in order to determine the mass profile, leading to loss of vital information. Since binning is impracticable for sparse samples, only galaxies with relatively rich systems of bright tracers, i.e. massive ETGs, are usually studied. This limitation also extends to X-ray-based studies, where X-ray haloes are observed mostly around massive galaxies that usually reside in dense environments. Hence most ETGs with radially extended mass modelling results in the literature are the more massive ones, with the low and intermediate mass ETGs usually overlooked. Furthermore, ETGs tend to be studied one at a time, with different methods and assumptions. This makes it problematic to compare the results in a systematic way.

Apart from the observational difficulties, results at large galactocentric radii in some intermediate mass ETGs ($M_* \sim 10^{11}\,M_\odot$) have suggested inconsistencies with the predictions from ΛCDM cosmology (e.g. Romanowsky et al. 2003; Napolitano et al. 2009; Deason et al. 2012, hereafter D+12). While results from the well-studied massive ETGs agree with the prediction that in the outer halo, DM dominates the galaxy mass budget, the same is less clear in intermediate mass ETGs, as different mass modelling techniques using the same tracers seem to produce contradictory results (see Romanowsky et al. 2003; Napolitano et al. 2009; D+12; Morganti et al. 2013, for the peculiar case of NGC 4494). The situation is even worse for low stellar mass ETGs, since they have hardly been studied out to large radii. It is therefore imperative to probe the DM halo in these galaxies systematically.

The traditional methods of mass modelling are difficult to apply to GC kinematic data for sub-L_* ETGs. It is therefore desirable to have mass estimators that use the projected kinematic information directly without the need for binning – an approach that lends itself to relatively sparse tracer populations. Examples include the virial mass estimator (VME) from Limber & Mathews (1960) and the projected mass estimator (PME) from Bahcall & Tremaine (1981), later modified by Heisler, Tremaine & Bahcall (1985). These assume that the tracers (e.g. GCs, PNe, satellite galaxies) have a number density distribution – $n(r)$, that directly follows the total mass density of the galaxy – $\rho(r)$, i.e. $n(r) \propto \rho(r)$. This is not usually true since the total mass density is dominated by the DM component, especially at large radii. The VME and PME are in principle similar to earlier attempts at estimating mass in a spherically symmetric, self-gravitating system where the tracers orbit a central point mass (e.g. Zwicky 1937; Schwarzschild 1954).

A more recent class of mass estimators, the tracer mass estimators (TMEs), however, allows for the more general case where the tracers and total mass densities, while both assumed to be scale-free, have different distributions. They were first introduced by Evans et al. (2003) and later modified by Watkins, Evans & An (2010, hereafter W+10), and (An & Evans 2011, see also Watkins et al. 2013 for an axisymmetric Jeans modelling of discrete kinematic tracers). A tracer population with number density $n(r) \propto r^{-\gamma}$ resides in a power-law gravitational potential of the form $\Phi(r) \propto r^{-\alpha}$. The total mass density, ρ, is directly related to the gravitational potential via Poisson's equation and hence it has the power-law form $\rho(r) \propto r^{-\alpha-2}$. Also, the TMEs assume that the tracer population is spherically symmetric and that galaxies are in steady-state equilibrium, i.e. virialized.

This paper uses the GC kinematic data from the SLUGGS[1] (SAGES Legacy Unifying Globulars and Galaxies Survey; Brodie et al. 2014) and TMEs to study in a homogeneous way the mass distribution within and beyond 5 R_e in ETGs. The galaxies we study cover a stellar mass range of 1.9×10^{10}–$4.0 \times 10^{11}\,M_\odot$ and include galaxies from cluster, group and field environments. We therefore extend the range of galaxies with mass profiles beyond 5 R_e into the low stellar mass galaxy regime. The science questions we seek to answer are straightforward – Are TMEs appropriate mass estimators using GCs as the tracers? How is mass distributed between baryons and DM in the outer haloes of ETGs, especially in intermediate and low stellar mass ETGs? Are ETGs always DM dominated in their outer parts? If they are not always DM dominated, as some results from the literature seem to suggest, then why? Are the measured mass and DM content estimates consistent with predictions from ΛCDM models?

In Section 2 we describe the observations, data reduction and data preparation. Section 3 starts by introducing in detail the TMEs, defines the mass estimator parameters and quantifies the sensitivity of the mass estimators to these parameters. In this section, we also quantify the effects of galaxy flattening, rotation and kinematic substructures on our mass estimates. We study the deviation of ETGs from isotropy. We obtain the DM fractions within 5 R_e and beyond, and compare with expectations from a simple galaxy model, composed of DM and stars only. In Section 4, we discuss how predictions and observations compare. We complete this section by studying correlations between the DM fraction and various galaxy properties. In Section 5, we summarize our results.

2 OBSERVATIONS, DATA REDUCTION AND DATA PRUNING

2.1 Observations and data reduction

The GC kinematic data used in this work were obtained through spectroscopic observations, mostly as part of the SLUGGS survey, with the DEIMOS (DEep Imaging Multi-Object Spectrograph; Faber et al. 2003) instrument on the 10 m Keck-II telescope. For NGC 3115, NGC 4486 and NGC 4649, we have supplemented our catalogue with data from some external sources (see Arnold et al. 2011; Strader et al. 2011; Pota et al. 2015, respectively, for details of these externally sourced kinematic data and the re-calibration of their uncertainties to match with those of DEIMOS). Spectroscopic data collection with DEIMOS began in 2006 and we have now obtained ∼3500 GC radial velocities in 25 carefully chosen ETGs (Brodie et al. 2014). Here, we only consider 23 galaxies from the SLUGGS survey with 20 or more spectroscopically confirmed GCs. Readers interested in a detailed explanation of our DEIMOS data reduction method are encouraged to check Pota et al. (2013) though we give a brief description here.

We design masks with 1 arcsec wide slits targeting GC candidates and integrate per mask for an average of 2 h. We set up DEIMOS

[1] http://sluggs.swin.edu.au

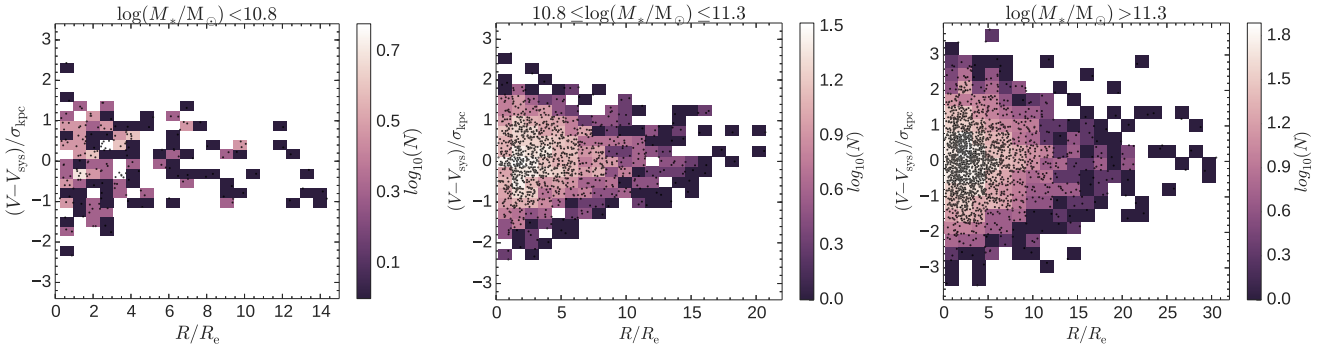

Figure 1. Line-of-sight velocities of the ∼3500 GCs in our sample of 23 galaxies normalized by their respective galaxy central velocity dispersion ($\sigma_{\rm kpc}$ from Table 2) versus galactocentric radius (in effective radius). The left-hand panel shows the low-mass galaxies (NGC 7457, NGC 3377 and NGC 4564), the middle panel shows intermediate mass galaxies (NGC 3608, NGC 4473, NGC 4278, NGC 821, NGC 3115, NGC 5866, NGC 1023, NGC 4494, NGC 4697, NGC 4697, NGC 1400, NGC 4526, NGC 2768 and NGC 3607), while the right-hand panel shows the high-mass galaxies (NGC 720, NGC 5846, NGC 4374, NGC 4365, NGC 4486, NGC 4649 and NGC 1407). GCs belonging to kinematic substructures have been excluded from this 2D histogram. The black dots are the individual GCs, while the colour bar shows the density of the points. On average, the GC line-of-sight velocities extend out to 13 $R_{\rm e}$ per galaxy. This figure is available in colour in the online version.

with the 1200 lines mm^{-1} centred on 7800 Å. This ensures we have a wavelength resolution of ∼1.5 Å and cover the CaT absorption lines in the near-infrared (8498, 8542, 8662 Å) and often the H α line at 6563 Å. We reduce our raw spectra using the IDL SPEC2D data reduction pipeline (Cooper et al. 2012) and obtain radial velocities by measuring the Doppler shifts of the CaT absorption lines using FXCOR task in IRAF. We cross-correlate our science spectra with spectral templates of 13 carefully chosen Galactic stars, obtained with the same instrument and setup. The final radial velocity for each object is the average from the cross-correlation. The uncertainties on our radial velocities are obtained by adding in quadrature the uncertainty outputs from FXCOR to the standard deviation among the templates, typically ∼3 km s^{-1}. Finally, our science spectra are redshift corrected.

To classify an object as a GC, we ensure that the CaT features in the rest-frame spectra are seen at the expected rest wavelength and the radial velocity is consistent with the host galaxy's systemic velocity (through a 3σ clipping implemented via the friendless algorithm of Merrett et al. (2003)). For secure classification as a GC, we require that at least the 8542 and 8662 Å CaT lines are observed, as well as the H α line (when the H α wavelength region is probed). In addition, we obtain a consensus from at least two members of the SLUGGS team on the status of our GC candidates. Objects with contentious status, but radial velocities consistent with the host galaxy's systemic velocity, are classified as *marginal* GCs. We do not use such objects in this work. Fig. 1 shows the composite galactocentric distribution of our homogeneous sample of ∼3500 GC line-of-sight velocities ($V_{\rm los}$) with well-understood errors used in this work. On average, our GC data extends to 10, 13 and 15 $R_{\rm e}$ in the low ($\log(M_*/{\rm M}_\odot) < 10.8$), intermediate ($10.8 \leq \log(M_*/{\rm M}_\odot) \leq 11.3$) and high ($\log(M_*/{\rm M}_\odot) > 11.3$) stellar mass galaxies in our sample, respectively.

2.2 Kinematic substructures in GC systems

A fundamental assumption of mass modelling methods is that the system of tracers is in dynamical equilibrium. However, if galaxies assembled their mass hierarchically via mergers and accretion events, a lumpy 'outer' halo is expected, especially in position–velocity phase space (Bullock & Johnston 2005; Helmi 2008; Cooper et al. 2013). The fossils of the accreted galaxies or satellite galaxies undergoing disruption that have not been totally phase mixed can sometimes be isolated in position–velocity phase space, even when the coherent structures are no longer evident in photometric studies. For the immediate task of mass modelling, it is important to isolate tracers that show correlations in position–velocity phase space, i.e. kinematic substructures, in order to avoid spurious mass estimates.

For each galaxy, we use the Dressler–Schectman (DS) test (Dressler & Shectman 1988; Ashman & Bird 1993; Pinkney et al. 1996; Mendel et al. 2008; Einasto et al. 2012) to detect substructures in position–velocity phase space and to quantify the significance of the substructures. For each GC, we compute the local average velocity ($\bar{V}_{\rm local}$) and velocity dispersion ($\sigma_{\rm local}$) using the $N_{\rm nn} = \sqrt{N_{\rm GC}}$ nearest neighbours (as advised by Pinkney et al. 1996). We then compare the local and global kinematics and sum over all the GCs to obtain Δ, the DS statistic, for the GC system using

$$\Delta = \sum_i \left\{ \left(\frac{N_{\rm nn}+1}{\sigma^2_{\rm global}} \right) \times [(\bar{V}_{{\rm local},i} - \bar{V}_{\rm global})^2 + (\sigma_{{\rm local},i} - \sigma_{\rm global})^2] \right\}^{1/2}. \quad (1)$$

For a Gaussian-like $V_{\rm los}$ distribution, Δ is approximately of the order of $N_{\rm GC}$ and the larger its value, the more likely it is that the GC system has substructures. However, a non-Gaussian $V_{\rm los}$ distribution can also produce a Δ significantly different from $N_{\rm GC}$ even when there are no real substructures. Therefore, to properly identify substructures and statistically quantify their significance, we perform a Monte Carlo experiment (repeated 5000 times) where we randomly shuffle the $V_{\rm los}$ of the GCs while keeping their positions fixed. This breaks any correlation between position and $V_{\rm los}$ while keeping the same velocity distribution and tests against the null hypothesis that there is no correlation between position and $V_{\rm los}$. The significance (p-value) is the number of times Δ from the Monte Carlo experiment is greater than that from the observed data divided by the total number of simulations, such that smaller p-values correspond to stronger substructure signatures. For GC systems with statistically significant substructures, i.e. p-val < 0.05, we identify and isolate the GCs with correlated kinematics and re-perform the DS test on the 'cleaned' data set iteratively until p-val > 0.05. The total numbers of GCs removed per GC system are summarized in Table 1. Table 2 contains the p-values for all the galaxies. We show the identified kinematic substructures from the DS test in Fig. 2.

Table 1. Summary of the spectroscopic observations for our galaxy sample.

Galaxy (NGC)	Masks	Exp. time (h)	N_{GC}	N_{sub}	R_{max} (R_e)
720	5	10.6	69	–	19.05
821	7	11.2	69	–	8.70
1023	4	8.8	115	21	16.15
1400	4	9.0	69	–	20.62
1407	10	22.0	372	–	14.14
2768	5	13.9	107	–	11.36
3115	5	14.0	150	12	18.35
3377	4	8.3	122	–	14.34
3608	5	9.9	36	–	9.75
4278	4	8.8	270	–	14.87
4365	6	9.0	251	–	12.90
4374	3	5.5	41	–	9.22
4473	4	2.8	106	–	17.35
4486	5	5.0	702	60	30.52
4494	5	4.6	107	10	8.52
4526	4	8.0	107	25	12.06
4564	3	4.5	27	–	8.33
4649	4	8.0	431	21	24.25
4697	1	2.0	20	–	4.66
5846	6	9.1	191	–	13.68
7457	4	7.5	40	6	6.26
3607	5	9.9	36	–	20.72
5866	1	2.0	20	–	5.75

Notes. The last two galaxies, NGC 3607 and NGC 5866, are *bonus* galaxies, in the sense that they were not originally included in the SLUGGS survey but we have obtained and analysed their data using the standard SLUGGS procedure. N_{GC} is the number of spectroscopically confirmed GCs per galaxy and N_{sub} is the number of GCs identified as belonging to kinematic substructures in Section 2.2. R_{max} shows the radial extent probed per galaxy in units of the effective radius, R_e.

We ensure that our final samples are free of substructures as identified by the DS test. We further compare mass estimates with and without the identified substructures in Section 3.5 to ascertain the effect of substructures on our mass estimation. However, we defer a detailed discussion of these substructures, within the context of hierarchical galaxy mass assembly, to a future paper.

3 ANALYSIS

3.1 TMEs

The TMEs are generally expressed as

$$M_p(<r_{out}) = \frac{C}{GN}\sum_{i=1}^{N} V_{los,i}^2 R_i^{\lambda}, \quad (2)$$

where r_{out} is the deprojected radius of the outermost GC, G is the gravitational constant and M_p is the pressure-supported mass, i.e. equation (2) assumes no rotation of the system. In practice r_{out} is taken as the projected galactocentric radius of the outermost GC. The prefactor C varies with TMEs but depends on the slope of the gravitational potential (α, see Section 3.2.1), the orbital distribution of the GCs (β, see Section 3.2.2) and the deprojected density profile of the GCs (γ, see Section 3.2.3). C is defined with two choices as

$$C = \begin{cases} \dfrac{16(\alpha+\gamma-2\beta)}{\pi(4-3\beta)} \dfrac{4-\alpha-\gamma}{3-\gamma} \dfrac{1-(r_{in}/r_{out})^{3-\gamma}}{1-(r_{in}/r_{out})^{4-\alpha-\gamma}} & \text{(i)} \\ \dfrac{(\alpha+\gamma-2\beta)}{I_{\alpha,\beta}} r_{out}^{1-\alpha} & \text{(ii)} \end{cases} \quad (3)$$

where r_{in} is the deprojected radius of the innermost GC and

$$I_{\alpha,\beta} = \frac{\pi^{1/2}\Gamma(\frac{\alpha}{2}+1)}{4\Gamma(\frac{\alpha}{2}+\frac{5}{2})}[\alpha+3-\beta(\alpha+2)] \quad (4)$$

with $\Gamma(x)$ being the gamma function. Equations (3) (i) and (ii) are from Evans et al. (2003) and W+10; An & Evans (2011), respectively. $\lambda \equiv 1$ in the TME of Evans et al. (2003) and $\lambda \equiv \alpha$ in those of W+10 and An & Evans (2011). Our kinematic data consist of N line-of-sight velocity ($V_{los,i}$) measurements at circularized galactocentric radii (R_i) defined as

$$R = \sqrt{qX^2 + \frac{Y^2}{q}}, \quad (5)$$

where q is the ratio of the galaxy photometric minor to major axis ($q = 1-\epsilon$), with X and Y as the projected Cartesian coordinates of individual GCs on the sky. Equation (5) is from Romanowsky et al. (2012), and it ensures that R_i is in a consistent format with the circularized effective radii (Cappellari et al. 2013b) we have used for our analysis.

The TME of W+10 has been shown to outperform that of Evans et al. (see W+10), and that of An et al. is just a special case of W+10 where $\gamma \equiv 3$. We therefore use the more general TME of W+10 for further analyses and hereafter refer to it as TME.

3.2 Defining α, β and γ

3.2.1 *The power-law slope of the gravitational potential – α*

In the TME formalism, the gravitational potential is described mathematically by a power-law function. This is assumed to be valid in the region probed and the slope is allowed to vary over $-1 \leq \alpha \leq 1$ such that

$$\Phi(r) \propto \begin{cases} \dfrac{v_0^2}{\alpha}\left(\dfrac{a}{r}\right)^{\alpha} & (\alpha \neq 0) \\ v_0^2 \log\left(\dfrac{a}{r}\right) & (\alpha = 0). \end{cases} \quad (6)$$

$\alpha = 0$ corresponds to an isothermal potential with a flat circular velocity curve (CVC) and $\alpha = 1$ corresponds to a Keplerian potential around a point mass, characterized by a declining CVC. v_0 is the circular velocity at *scale radius* a.

The power-law slope of the gravitational potential is a priori unknown and in the following we use different assumptions based on observations and/or theory to constrain our choice of α. The simplest clue about α is to be found from recent studies (e.g. Auger et al. 2010; Thomas et al. 2011; Cappellari et al. 2015) where the total mass density of ETGs was found to be *nearly* isothermal with a small intrinsic scatter, i.e. $\rho(r) \propto r^{-2}$. These studies therefore suggest that $\alpha \sim 0$. However, there are indications of a trend in the logarithmic slope of the total mass density profiles for ETGs with the more (less) massive ETGs having shallower (steeper) slopes both observationally (e.g. Barnabè et al. 2011; D+12; Tortora et al. 2014) and from cosmological simulations (e.g. Dutton et al. 2013; Remus et al. 2013). This implies that a variety of shapes would be seen in the CVCs at large radii.

Under the assumption of a power-law gravitational potential, α can be evaluated (see Evans 1994) as the logarithmic slope of the CVC at large radii

$$\alpha \equiv -\lim_{R\to\infty} \frac{\mathrm{d}\log V_c^2}{\mathrm{d}\log R}. \quad (7)$$

Using equation (7) we determine α given the CVCs from the cosmological hydrodynamical resimulations of Oser et al. (2010,

Table 2. General properties of our galaxies. Column description: (1) galaxy name; (2) total extinction-corrected K-band magnitude, obtained using the absolute K-band magnitude from 2MASS (Jarrett et al. 2000), dust extinction correction from Schlegel, Finkbeiner & Davis (1998) and the correction to the 2MASS photometry due to sky oversubtraction from Scott, Graham & Schombert (2013); (3)–(8) are from Brodie et al. (2014) and include (3) distance; (4) systemic velocity; (5) effective (half-light) radius; (6) central stellar velocity dispersion within 1 kpc; (7) ellipticity and (8) environmental density of neighbouring galaxies; (9) total logarithmic stellar mass, obtained from the absolute K-band magnitude, assuming $M/L_K = 1$ (here and elsewhere in the paper, stellar M/L ratio is quoted in units of $M_\odot/L_{\odot,K}$); typical uncertainties on our stellar masses are ∼0.15 dex.; (10) statistical significance of having kinematic substructures in GC system [see Section 2.2 for derivation of column (10)]; (11) the power-law slope of the gravitational potential; (12) the power-law slope of the deprojected GC density profile [see Section 3.2 for derivation of columns (11) and (12)]; (13) normalizing factor to correct for effect of galaxy flattening on dynamical mass estimate and (14) rotation dominance parameter for the GC system, after removing kinematic substructures where relevant [see Section 3.4 for columns (13) and (14)].

Galaxy (NGC) (1)	M_K (mag) (2)	Dist. (Mpc) (3)	$V_{\rm sys}$ (km s^{-1}) (4)	$R_{\rm e}$ (arcsec) (5)	$\sigma_{\rm kpc}$ (km s^{-1}) (6)	ϵ (7)	$\rho_{\rm env}$ (Mpc^{-3}) (8)	$\log(M_*/M_\odot)$ (9)	p-val (10)	α (11)	γ (12)	corr (13)	$V_{\rm rot}/\sigma$ (14)
720	−25.09	26.9	1745	35	227	0.49	0.25	11.35	0.051	0.058	2.66	0.92	$0.42^{+0.24}_{-0.17}$
821	−24.14	23.4	1718	40	193	0.35	0.08	10.97	0.411	0.234	2.90	0.98	$0.40^{+0.20}_{-0.18}$
1023	−24.16	11.1	602	48	183	0.63	0.57	10.98	<0.009	0.230	2.89	0.85	$0.65^{+0.21}_{-0.18}$
1400	−24.53	26.8	558	28	236	0.13	0.07	11.12	0.288	0.163	2.80	1.01	$0.22^{+0.20}_{-0.15}$
1407	−25.72	26.8	1779	63	252	0.07	0.42	11.60	0.106	−0.056	2.60	1.01	$0.04^{+0.08}_{-0.07}$
2768	−24.91	21.8	1353	63	206	0.57	0.31	11.28	0.364	0.092	2.70	0.88	$0.50^{+0.15}_{-0.15}$
3115	−24.15	9.4	663	35	248	0.66	0.08	10.97	0.043	0.232	2.89	0.83	$0.94^{+0.15}_{-0.16}$
3377	−22.83	10.9	690	36	135	0.33	0.49	10.44	0.419	0.477	3.23	0.98	$0.23^{+0.14}_{-0.10}$
3608	−23.78	22.3	1226	30	179	0.20	0.56	10.82	0.953	0.301	2.99	1.01	$0.21^{+0.26}_{-0.18}$
4278	−23.93	15.6	620	32	228	0.09	1.25	10.88	0.73	0.273	2.95	1.01	$0.13^{+0.08}_{-0.07}$
4365	−25.43	23.1	1243	53	253	0.24	2.93	11.48	0.195	−0.003	2.57	1.00	$0.15^{+0.10}_{-0.08}$
4374	−25.36	18.5	1017	53	284	0.05	3.99	11.46	0.472	0.009	2.59	1.01	$0.45^{+0.25}_{-0.24}$
4473	−23.90	15.2	2260	27	189	0.43	2.17	10.87	0.537	0.279	2.96	0.95	$0.23^{+0.15}_{-0.11}$
4486	−25.55	16.7	1284	81	307	0.16	4.17	11.53	<0.001	−0.027	2.54	1.01	$0.14^{+0.06}_{-0.05}$
4494	−24.27	16.6	1342	49	157	0.14	1.04	11.02	0.018	0.210	2.86	1.01	$0.51^{+0.15}_{-0.14}$
4526	−24.81	16.4	617	45	233	0.76	2.45	11.23	<0.001	0.111	2.73	0.77	$0.61^{+0.23}_{-0.24}$
4564	−23.17	15.9	1155	20	153	0.53	4.09	10.58	0.054	0.414	3.14	0.90	$1.80^{+0.51}_{-0.33}$
4649	−25.61	16.5	1110	66	308	0.16	3.49	11.56	<0.001	−0.037	2.53	1.01	$0.34^{+0.07}_{-0.08}$
4697	−24.29	12.5	1252	62	180	0.32	0.60	11.03	0.394	0.206	2.86	0.98	$2.37^{+0.83}_{-0.86}$
5846	−25.22	24.2	1712	59	231	0.08	0.84	11.40	0.553	0.034	2.62	1.01	$0.08^{+0.09}_{-0.07}$
7457	−22.42	12.9	844	36	74	0.47	0.13	10.28	0.014	0.552	3.33	0.93	$1.90^{+0.53}_{-0.42}$
3607	−24.96	22.2	942	39	229	0.13	0.34	11.29	0.227	0.084	2.69	1.01	$0.18^{+0.22}_{-0.15}$
5866	−24.15	14.9	755	36	163	0.58	0.24	10.97	0.978	0.232	2.89	0.88	$0.16^{+1.06}_{-0.36}$

2012). We use the logarithmic slopes of their CVCs as analysed by Wu et al. (2014, hereafter Wu+14), in 42 of these simulated ETGs. The simulated ETGs have stellar masses over the range 2.7×10^{10}–4.7×10^{11} $M_\odot$, comparable to the stellar mass range in this study. The logarithmic slope is evaluated at 5 $R_{\rm e}$. We find an empirical relation between α and the logarithm of the stellar mass by fitting a linear function to the data (see Fig. 3). The best-fitting linear function to the data is

$$\alpha = (-0.46 \pm 0.06) \times \log(M_*/M_\odot) + (5.29 \pm 0.68) \quad (8)$$

with an rms scatter of 0.13 ± 0.01. Using equation (7) and the radially extended CVC data (out to 20 kpc) for ETGs published in Trujillo-Gomez et al. (2011), we confirm that the relation obtained above is consistent with observations in the region of overlap. Our best-fitting function is similar to those reported in Tortora et al. (2014) determined at much more central radii of 0.5 and 1 $R_{\rm e}$. When constrained this way, α reflects the shallower (steeper) total mass density profiles for more (less) massive ETGs. With equation (8), $\alpha \sim 0.4$ for an arbitrary galaxy with MW-like stellar mass, consistent with the results for the Galaxy potential in Yencho et al. (2006) and W+10. Table 2 contains a summary of α adopted for the galaxies in this study, given their stellar mass.

3.2.2 *The orbital anisotropy parameter – β*

The Binney anisotropy parameter, β, (Binney & Tremaine 1987) describes the orbital distribution of the GCs. It can be a major source of uncertainty in mass modelling of ETGs as it is poorly constrained. It is defined (assuming spherical symmetry) as

$$\beta = 1 - \frac{\sigma_\theta^2}{\sigma_r^2}, \quad (9)$$

where σ_θ and σ_r are the tangential and radial velocity dispersions, respectively. The TMEs are based on the assumption of constant anisotropy with radius. We do not fit for β, but rather we derive mass estimates assuming $\beta = 0, 0.5, -0.5$, corresponding to isotropic, strong radial and mild tangential anisotropies, respectively. Our choice of ±0.5 is predicated on results from mass modelling where

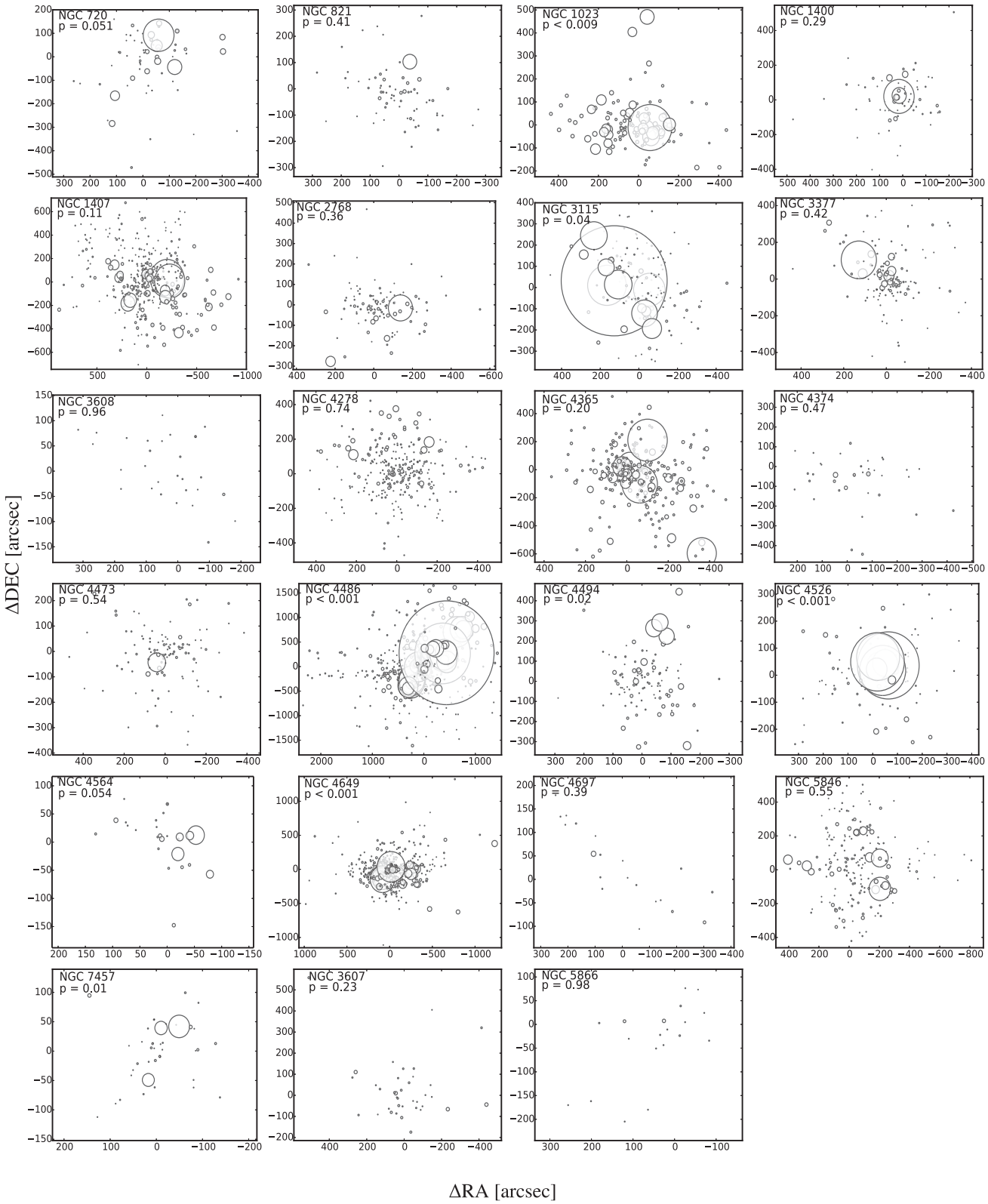

Figure 2. GC bubble diagrams from the DS substructure test. The circles represent the GCs and have been scaled to show the differences between local and global kinematics, such that bigger circles show higher probability of kinematic substructures. Galaxy ID and statistical significance of the identified substructures are shown on each plot (the smaller the p-value, the higher the significance of the substructure). North is up and east is left in all the plots.

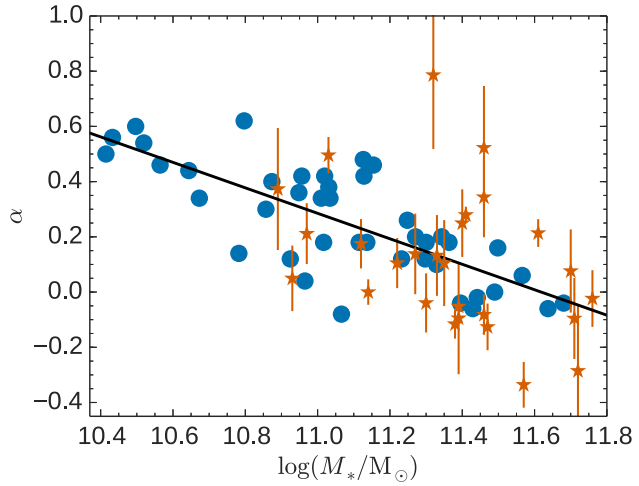

Figure 3. The power-law slope of the gravitational potential, α versus galaxy stellar mass. The blue circles are from the simulated ETGs in Wu+14, while the brown stars are from the observational data published in Trujillo-Gomez et al. (2011). The solid line is the best fit to the predictions from Wu+14.

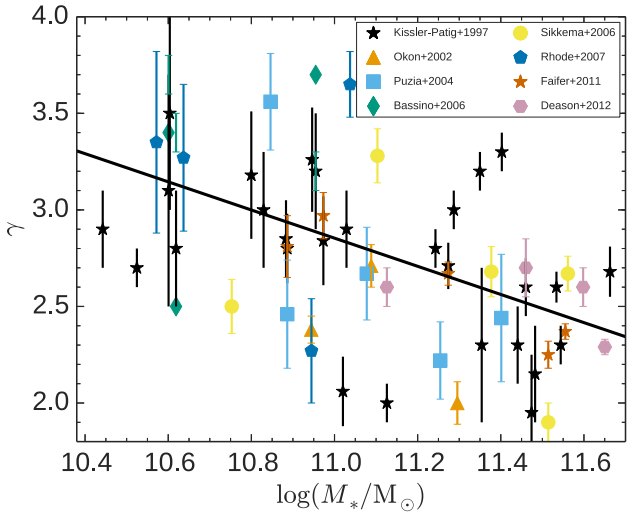

Figure 4. The power-law slope of the deprojected GC density profile, γ versus galaxy stellar mass. Data points are from Kissler-Patig (1997), Okoń & Harris (2002), Puzia et al. (2004), Bassino, Richtler & Dirsch (2006), Sikkema et al. (2006), Rhode et al. (2007), Faifer et al. (2011) and D+12, as summarized in the plot legend. The solid line is a linear fit to all of the data.

typical anisotropies are usually defined such that $-0.5 \leq \beta \leq 0.5$ (Gerhard et al. 2001; Cappellari et al. 2007). We show in Section 3.3 the sensitivity of our mass estimates to this parameter.

3.2.3 The power-law slope of the deprojected GC density profile – γ

We follow Harris (1976) and derive the deprojected GC density distribution $n(r) \sim r^{-\gamma}$ given the projected density profiles of photometric GCs in the plane of the sky, i.e. $N(R) \sim R^{-(\gamma\,-\,1)}$. It is well known that the slope of the GC surface density profile varies with the galaxy luminosity (e.g. Harris 1986; Kissler-Patig 1997; Dirsch, Schuberth & Richtler 2005; Bekki & Forbes 2006). We therefore make a compilation of measured slopes of the GC density profiles (which we de-project) from wide-field photometric studies in the literature (Kissler-Patig 1997; Okoń & Harris 2002; Puzia et al. 2004; Bassino et al. 2006; Sikkema et al. 2006; Rhode et al. 2007; Faifer et al. 2011; D+12) and the corresponding stellar mass of the host galaxy (using distance from Tonry et al. 2001; Blakeslee et al. 2009; Brodie et al. 2014, the absolute K-band magnitude from 2MASS, the correction from Scott et al. 2013 and assuming a stellar $M/L_K = 1$). Fig. 4 shows the deprojected power-law slopes as a function of galaxy stellar mass. The best-fitting linear function to the data is

$$\gamma = (-0.63 \pm 0.17) \times \log(M_*/\mathrm{M}_\odot) + (9.81 \pm 1.94) \qquad (10)$$

with an rms scatter of 0.29 ± 0.04 in the data around the best-fitting line. With this linear relation we estimate the deprojected slope of the GC density profile of a galaxy given its stellar mass. This is a useful tool when the photometric data are not readily available. Table 2 contains a summary of γ for all the galaxies in this study.

The power-law slope of the deprojected GC density profile is thus constrained to $2 \leq \gamma \leq 4$, with more massive ETGs having shallower profiles and lower mass ETGs showing steeper profiles. For a galaxy with MW-like stellar mass, we find $\gamma = 3.3$, similar to that of the Galaxy, ∼3.5 (Harris 1976; W+10).

3.3 Sensitivity of pressure-supported mass estimates to α, β and γ

We investigate the effects of the adopted values of α, β and γ on the pressure-supported mass estimates, M_p, from equation (2), using NGC 1407 as a test case. Di Cintio et al. (2012) showed that while the variations in M_p due to uncertainties in γ and β can be generalized, that due to changes in α is a complicated function (see their equation 19) that varies from galaxy to galaxy, depending on the radial distribution of the tracers. Fig. 5 shows M_p within 5 R_e for NGC 1407. For our sensitivity tests, we extend the range of β out to ± 1 to study mass–anisotropy dependences at more extreme values. The *left-hand panel* shows M_p when $\gamma \equiv 3$, $-0.1 \leq \alpha \leq 0.5$ and $-1.0 \leq \beta \leq 1.0$. In the *middle panel*, $\alpha \equiv 0$, $2 \leq \gamma \leq 4$ and $-1.0 \leq \beta \leq 1.0$. The two plots reveal that mass estimates are least sensitive to β and most sensitive to the assumed potential slope, α. For example, a 0.5 change in γ when $\beta = 0$ and $\alpha = 0$ alters the mass estimate by ∼20 per cent, while a change of 0.1 in α at $\beta = 0$ and $\gamma = 3$ changes the mass by ∼30 per cent. Ignorance of the nature of β becomes an increasingly important issue only when the orbital distribution of the tracers is strongly radial, i.e. $\beta \geq 0.5$. We have also performed this test on all the other galaxies in the sample and confirm that in all cases M_p is most sensitive to α and least sensitive to β.

For galaxies with nearly isothermal gravitational potentials, radially biased orbital distributions increasingly lead to lower total mass estimates. However, in strongly Keplerian potentials, radially biased orbital distributions would lead to higher mass estimates. This implies that when $\alpha + \gamma < 3$, the total mass obtained under the assumption of tangential anisotropy is greater than that obtained assuming radial anisotropy. In the same way, when $\alpha + \gamma > 3$, the total mass obtained under the assumption of tangential anisotropy is less than that obtained assuming radial anisotropy. This is the classic situation from dynamical modelling studies with stars and PN in the far outer haloes e.g. (Dekel et al. 2005). When $\alpha + \gamma \sim 3$, the mass estimates are insensitive to β, similar to the result reported in Wolf et al. (2010) for pressure supported galaxies. Also,

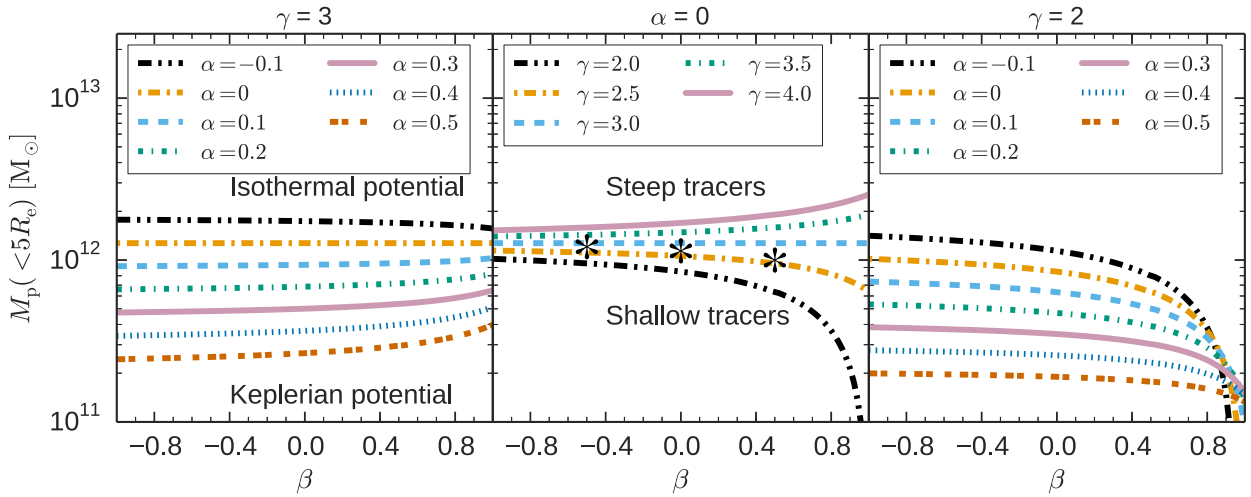

Figure 5. Sensitivity of pressure-supported mass estimate for NGC 1407 within 5 effective radii to parameters α, β and γ. Left-hand panel: mass estimate when $\gamma \equiv 3$, with $-0.1 \leq \alpha \leq 0.5$ and $-1.0 \leq \beta \leq 1.0$. A 0.1 change in α at $\beta = 0$ and $\gamma = 3$ corresponds to a change in the mass estimate of ∼30 per cent. Middle panel: mass estimate when $\alpha \equiv 0$, with $2.0 \leq \gamma \leq 4.0$ and $-1.0 \leq \beta \leq 1.0$. A change of 0.5 in γ at $\beta = 0$ and $\alpha = 0$ changes the mass estimate by ∼20 per cent. Mass estimates significantly diverge for $\beta = 0.5$, with strongly radial orbital distributions producing extremely divergent mass estimates. Note that when $\alpha + \gamma = 3$, mass estimates are very insensitive to β. The asterisks show the pressure-supported mass estimates for NGC 1407 when β is −0.5, 0, 0.5, respectively. Right-hand panel: at the shallow limit of the power-law slope of the mass tracers (i.e. $\gamma = 2$) and isothermal gravitational potential (i.e. $\alpha \sim 0$), strongly radial orbits produce degenerate mass estimates. This figure is available in colour in the online version.

when $\beta \to 1$ (see *right-hand panel*), particularly for galaxies with an isothermal gravitational potential, i.e. more massive ellipticals, the mass estimates become degenerate (see also Wolf et al. 2010). The typical α and γ pairs adopted for the low-, intermediate- and high-mass galaxies in our sample are (0.4, 3.4), (0.2, 2.9) and (0, 2.6), respectively.

3.4 Quantifying the effects of galaxy flattening and GC rotation on mass estimates

The TMEs are built on the assumption that galaxies are spherically symmetric and pressure supported. However, these assumptions are not always *valid* and mass estimates thus need to properly account for other realities. Edge-on and face-on galaxies, under the sphericity assumption, would have their masses overestimated or underestimated, respectively (see Bacon 1985; Bender, Saglia & Gerhard 1994; Magorrian & Ballantyne 2001), closely mimicking the mass–anisotropy degeneracy. A flattening-based mass correction of some sort is therefore necessary. Galaxies in our sample have been deliberately chosen with a bias towards edge-on inclinations to reduce confusion in mass estimates from projection effects, hence we are affected more by *overestimation*. We apply the normalizing factor from Bacon 1985 to correct for the effect of galaxy flattening on our dynamical mass estimates (their equation 9), assuming that GC systems have the same ellipticity as the galaxy stars. We multiply our mass estimate M_p (obtained under the assumption of sphericity, i.e. $q' \sim 1$), from equation (2), by a factor corr to normalize to mass when $q = 1 - \epsilon$. We use

$$\mathrm{corr}(q', q) = \left(\frac{e'}{e}\right)^{-3} \times \frac{(sin^{-1}e' - e'q')(1-q^2) - 2q'^2(sin^{-1}e' - e'/q')(q^2 - q'^2)}{(1-q'^2)(sin^{-1}e - eq)}, \quad (11)$$

where $e' = (1 - q')^{1/2}$ and $e = (1 - q)^{1/2}$.

Fig. 6 shows the effects of galaxy flattening on the total mass estimates within 5 R_e after applying the correction from equation (11).

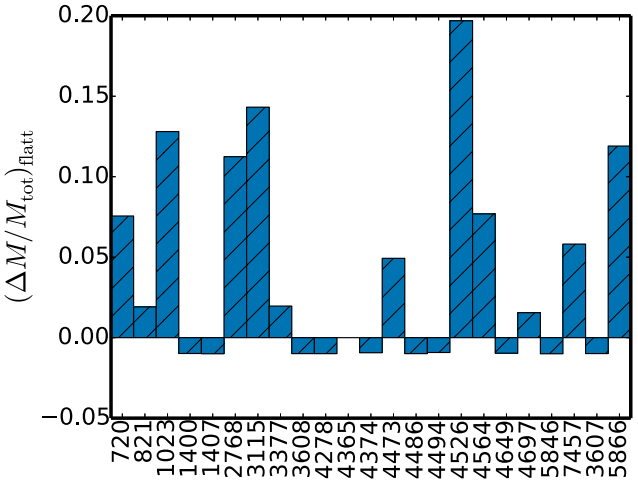

Figure 6. Bar chart showing effect of galaxy flattening on the total dynamical mass within 5 R_e. For our galaxy sample, we are largely affected by mass overestimation, with an average mass overestimation due to galaxy flattening of ∼5 per cent.

The average difference in total mass estimates due to galaxy flattening is ∼5 per cent. This reflects the bias of our galaxy sample in favour of edge-on galaxies. We note that the severity of the overestimation is highest for NGC 4526 (with $\epsilon = 0.76$, where the total mass would have been overestimated by ∼20 per cent). We list the correction factors so obtained for each galaxy in Table 2 and report dynamical mass estimates corrected for galaxy flattening in Table 3.

Similarly, dynamical masses obtained under the assumption of non-rotating tracers would be largely underestimated for galaxies where the tracer population has kinematics dominated by rotation. Flattened (discy) ETGs have been shown to be mostly fast central rotators (Krajnović et al. 2011), with some of them observed to remain fast rotators even at large radii (e.g. Arnold et al. 2014). This result has been confirmed in studies that probed the kinematics of

Table 3. Summary of mass estimates and DM fractions assuming different anisotropy. The results shown here have been obtained using the TME of W+10 (see Section 3.1 for details) and assuming stellar $M/L_K = 1$. M_p is the pressure-supported mass and it has been corrected for the effect of galaxy flattening. M_{rot} is the rotationally supported mass. M_{tot} is the total dynamical mass after correcting for galaxy flattening, rotation in the GC system and the presence of kinematic substructures (for galaxies with $p < 0.05$). f_{DM} is the DM fraction. We list masses enclosed within spheres of radius 5 R_e and R_{max}, the maximum galactocentric radius where we have GC kinematic data.

Galaxy (NGC)	β	$M_{rot}(<5\,R_e)$ ($10^{10}\,M_\odot$)	$M_p(<5R_e)$ ($10^{11}\,M_\odot$)	$M_{tot}(<5\,R_e)$ ($10^{11}\,M_\odot$)	$f_{DM}(<5\,R_e)$	R_{max} (R_e)	$M_{rot}(<R_{max})$ ($10^{10}\,M_\odot$)	$M_p(<R_{max})$ ($10^{11}\,M_\odot$)	$M_{tot}(<R_{max})$ ($10^{11}\,M_\odot$)	$f_{DM}(<R_{max})$
720	0	2.0 ± 0.4	3.4 ± 0.8	3.6 ± 0.7	0.46 ± 0.16	19.05	7.6 ± 1.4	11.9 ± 2.4	12.7 ± 2.2	0.83 ± 0.05
	0.5		3.3 ± 0.7	3.5 ± 0.7	0.43 ± 0.19		7.6 ± 1.4	11.3 ± 2.2	12.1 ± 2.1	0.82 ± 0.05
	−0.5		3.5 ± 0.8	3.7 ± 0.7	0.47 ± 0.16		7.6 ± 1.4	12.1 ± 2.4	12.9 ± 2.2	0.83 ± 0.05
821	0	1.9 ± 0.4	4.0 ± 0.8	4.2 ± 0.8	0.81 ± 0.06	8.70	3.4 ± 0.7	5.6 ± 1.0	6.0 ± 1.0	0.85 ± 0.04
	0.5		4.2 ± 0.8	4.4 ± 0.8	0.81 ± 0.06		3.4 ± 0.7	5.8 ± 1.1	6.2 ± 1.1	0.86 ± 0.04
	−0.5		4.0 ± 0.8	4.2 ± 0.8	0.8 ± 0.06		3.4 ± 0.8	5.5 ± 1.0	5.9 ± 1.0	0.85 ± 0.04
1023	0	2.4 ± 0.4	1.4 ± 0.3	1.6 ± 0.2	0.48 ± 0.13	16.15	7.7 ± 1.4	3.2 ± 0.6	4.0 ± 0.5	0.76 ± 0.05
	0.5		1.5 ± 0.3	1.7 ± 0.2	0.49 ± 0.12		7.7 ± 1.4	3.3 ± 0.6	4.1 ± 0.5	0.77 ± 0.05
	−0.5		1.4 ± 0.3	1.6 ± 0.2	0.47 ± 0.12		7.7 ± 1.4	3.1 ± 0.6	3.9 ± 0.5	0.76 ± 0.05
1400	0	0.4 ± 0.1	2.3 ± 0.5	2.3 ± 0.5	0.5 ± 0.19	20.62	1.6 ± 0.6	7.2 ± 1.3	7.4 ± 1.3	0.82 ± 0.04
	0.5		2.3 ± 0.5	2.4 ± 0.5	0.5 ± 0.18		1.6 ± 0.6	7.2 ± 1.3	7.4 ± 1.3	0.82 ± 0.05
	−0.5		2.3 ± 0.5	2.3 ± 0.6	0.49 ± 0.23		1.6 ± 0.6	7.2 ± 1.3	7.3 ± 1.3	0.82 ± 0.05
1407	0	0.1 ± 0.0	11.5 ± 1.1	11.5 ± 1.1	0.71 ± 0.06	14.14	0.2 ± 0.1	36.6 ± 2.7	36.6 ± 2.6	0.9 ± 0.02
	0.5		10.2 ± 1.0	10.2 ± 1.0	0.67 ± 0.07		0.2 ± 0.1	32.3 ± 2.4	32.3 ± 2.3	0.88 ± 0.02
	−0.5		12.2 ± 1.2	12.2 ± 1.2	0.72 ± 0.06		0.2 ± 0.1	38.7 ± 2.8	38.7 ± 2.9	0.9 ± 0.02
2768	0	4.5 ± 0.4	6.7 ± 1.1	7.1 ± 1.0	0.77 ± 0.07	11.36	10.3 ± 0.9	13.1 ± 2.1	14.1 ± 1.8	0.87 ± 0.04
	0.5		6.5 ± 1.1	6.9 ± 0.9	0.76 ± 0.07		10.3 ± 0.9	12.7 ± 2.0	13.7 ± 1.8	0.87 ± 0.04
	−0.5		6.8 ± 1.1	7.2 ± 1.0	0.77 ± 0.07		10.3 ± 0.8	13.3 ± 2.1	14.3 ± 1.8	0.87 ± 0.04
3115	0	3.2 ± 0.6	1.7 ± 0.3	2.0 ± 0.3	0.57 ± 0.08	18.35	11.8 ± 2.3	4.5 ± 0.7	5.7 ± 0.6	0.83 ± 0.02
	0.5		1.8 ± 0.3	2.1 ± 0.3	0.58 ± 0.07		11.8 ± 2.3	4.6 ± 0.7	5.8 ± 0.6	0.84 ± 0.02
	−0.5		1.7 ± 0.3	2.0 ± 0.3	0.56 ± 0.09		11.8 ± 2.2	4.4 ± 0.6	5.6 ± 0.6	0.83 ± 0.02
3377	0	0.1 ± 0.1	0.6 ± 0.1	0.6 ± 0.1	0.58 ± 0.08	14.34	0.3 ± 0.2	1.2 ± 0.2	1.3 ± 0.2	0.79 ± 0.04
	0.5		0.7 ± 0.1	0.7 ± 0.1	0.63 ± 0.07		0.3 ± 0.1	1.4 ± 0.2	1.5 ± 0.2	0.81 ± 0.03
	−0.5		0.6 ± 0.1	0.6 ± 0.1	0.55 ± 0.1		0.3 ± 0.1	1.2 ± 0.2	1.2 ± 0.2	0.77 ± 0.04
3608	0	0.3 ± 0.2	3.3 ± 1.1	3.4 ± 1.1	0.82 ± 0.18	9.75	0.7 ± 0.4	4.3 ± 1.2	4.4 ± 1.2	0.85 ± 0.08
	0.5		3.6 ± 1.1	3.6 ± 1.2	0.83 ± 0.26		0.7 ± 0.4	4.6 ± 1.3	4.7 ± 1.3	0.86 ± 0.07
	−0.5		3.2 ± 1.0	3.3 ± 1.1	0.82 ± 0.6		0.7 ± 0.4	4.2 ± 1.2	4.3 ± 1.1	0.85 ± 0.06
4278	0	0.2 ± 0.1	2.8 ± 0.3	2.8 ± 0.4	0.75 ± 0.06	14.87	0.5 ± 0.2	6.5 ± 0.6	6.5 ± 0.6	0.88 ± 0.02
	0.5		2.9 ± 0.4	3.0 ± 0.4	0.76 ± 0.06		0.5 ± 0.2	6.9 ± 0.6	6.9 ± 0.6	0.89 ± 0.02
	−0.5		2.7 ± 0.3	2.7 ± 0.3	0.74 ± 0.06		0.5 ± 0.2	6.3 ± 0.5	6.4 ± 0.6	0.88 ± 0.03
4365	0	1.0 ± 0.2	12.0 ± 1.3	12.1 ± 1.3	0.78 ± 0.05	12.90	2.6 ± 0.5	29.5 ± 2.6	29.8 ± 2.7	0.9 ± 0.02
	0.5		11.0 ± 1.2	11.1 ± 1.2	0.76 ± 0.05		2.6 ± 0.5	27.0 ± 2.4	27.3 ± 2.5	0.89 ± 0.02
	−0.5		12.5 ± 1.3	12.6 ± 1.4	0.79 ± 0.05		2.6 ± 0.5	30.8 ± 2.8	31.1 ± 2.8	0.91 ± 0.02
4374	0	8.8 ± 2.0	13.2 ± 3.4	14.1 ± 3.3	0.82 ± 0.06	9.22	16.2 ± 3.7	21.0 ± 4.8	22.6 ± 4.8	0.88 ± 0.04
	0.5		12.2 ± 3.1	13.1 ± 3.1	0.81 ± 0.07		16.2 ± 3.9	19.4 ± 4.5	21.0 ± 4.5	0.87 ± 0.04
	−0.5		13.7 ± 3.5	14.6 ± 3.7	0.83 ± 0.07		16.2 ± 3.6	21.8 ± 5.0	23.4 ± 5.1	0.88 ± 0.04
4473	0	0.2 ± 0.1	1.4 ± 0.3	1.4 ± 0.3	0.52 ± 0.12	17.35	0.8 ± 0.4	3.6 ± 0.5	3.6 ± 0.5	0.8 ± 0.04
	0.5		1.5 ± 0.3	1.5 ± 0.3	0.55 ± 0.12		0.8 ± 0.4	3.8 ± 0.6	3.9 ± 0.5	0.81 ± 0.04
	−0.5		1.4 ± 0.3	1.4 ± 0.3	0.51 ± 0.12		0.8 ± 0.4	3.5 ± 0.5	3.5 ± 0.5	0.79 ± 0.04
4486	0	1.6 ± 0.2	24.0 ± 1.7	24.2 ± 1.8	0.88 ± 0.01	30.52	9.8 ± 1.1	146.0 ± 8.2	147.0 ± 8.1	0.98 ± 0.0
	0.5		21.6 ± 1.6	21.8 ± 1.6	0.86 ± 0.01		9.8 ± 1.1	131.0 ± 7.4	132.0 ± 7.2	0.97 ± 0.0
	−0.5		25.2 ± 1.8	25.4 ± 1.9	0.88 ± 0.01		9.8 ± 1.1	153.0 ± 8.6	154.0 ± 8.6	0.98 ± 0.0
4494	0	1.2 ± 0.1	1.4 ± 0.2	1.5 ± 0.2	0.39 ± 0.12	8.52	2.0 ± 0.3	1.9 ± 0.3	2.1 ± 0.3	0.53 ± 0.09
	0.5		1.4 ± 0.2	1.6 ± 0.2	0.41 ± 0.12		2.0 ± 0.2	2.0 ± 0.3	2.2 ± 0.3	0.54 ± 0.08
	−0.5		1.4 ± 0.2	1.5 ± 0.2	0.38 ± 0.13		2.0 ± 0.2	1.9 ± 0.3	2.1 ± 0.3	0.52 ± 0.09
4526	0	2.9 ± 0.6	3.1 ± 0.8	3.4 ± 0.6	0.56 ± 0.14	12.06	7.0 ± 1.5	6.5 ± 1.3	7.2 ± 1.1	0.77 ± 0.06
	0.5		3.1 ± 0.8	3.4 ± 0.6	0.55 ± 0.14		7.0 ± 1.4	6.4 ± 1.3	7.1 ± 1.0	0.77 ± 0.06
	−0.5		3.2 ± 0.8	3.5 ± 0.6	0.56 ± 0.13		7.0 ± 1.4	6.6 ± 1.4	7.3 ± 1.1	0.77 ± 0.06
4564	0	2.4 ± 0.4	0.8 ± 0.3	1.0 ± 0.2	0.65 ± 0.17	8.33	4.0 ± 0.7	0.9 ± 0.3	1.3 ± 0.3	0.72 ± 0.1
	0.5		0.9 ± 0.3	1.1 ± 0.3	0.68 ± 0.13		4.0 ± 0.6	1.0 ± 0.3	1.4 ± 0.3	0.74 ± 0.08
	−0.5		0.7 ± 0.2	1.0 ± 0.2	0.64 ± 0.16		4.0 ± 0.6	0.9 ± 0.3	1.3 ± 0.3	0.71 ± 0.09

Table 3 – *continued*

Galaxy (NGC)	β	$M_{\rm rot}(<5\,R_{\rm e})$ ($10^{10}\,{\rm M}_{\odot}$)	$M_{\rm p}(<5\,R_{\rm e})$ ($10^{11}\,{\rm M}_{\odot}$)	$M_{\rm tot}(<5\,R_{\rm e})$ ($10^{11}\,{\rm M}_{\odot}$)	$f_{\rm DM}(<5\,R_{\rm e})$	$R_{\rm max}$ ($R_{\rm e}$)	$M_{\rm rot}(<R_{\rm max})$ ($10^{10}\,{\rm M}_{\odot}$)	$M_{\rm p}(<R_{\rm max})$ ($10^{11}\,{\rm M}_{\odot}$)	$M_{\rm tot}(<R_{\rm max})$ ($10^{11}\,{\rm M}_{\odot}$)	$f_{\rm DM}(<R_{\rm max})$
4649	0	3.8 ± 0.3	10.9 ± 0.9	11.3 ± 0.9	0.72 ± 0.05	24.25	18.6 ± 1.6	53.8 ± 3.8	55.7 ± 3.7	0.94 ± 0.01
	0.5		9.8 ± 0.8	10.2 ± 0.8	0.69 ± 0.06		18.6 ± 1.6	48.2 ± 3.4	50.1 ± 3.4	0.93 ± 0.01
	−0.5		11.5 ± 0.9	11.9 ± 1.0	0.74 ± 0.05		18.6 ± 1.6	56.6 ± 4.0	58.5 ± 4.1	0.94 ± 0.01
4697	0	20.3 ± 3.4	7.0 ± 2.4	9.1 ± 2.4	0.9 ± 0.04	4.66	–	–	–	–
	0.5		7.2 ± 2.4	9.3 ± 2.4	0.9 ± 0.05		–	–	–	–
	−0.5		6.9 ± 2.3	9.0 ± 2.3	0.9 ± 0.04		–	–	–	–
5846	0	0.3 ± 0.1	12.4 ± 1.6	12.4 ± 1.7	0.83 ± 0.05	13.68	0.8 ± 0.2	32.6 ± 3.5	32.7 ± 3.5	0.93 ± 0.02
	0.5		11.6 ± 1.5	11.6 ± 1.5	0.81 ± 0.05		0.8 ± 0.2	30.6 ± 3.3	30.7 ± 3.2	0.92 ± 0.02
	−0.5		12.8 ± 1.7	12.8 ± 1.7	0.83 ± 0.04		0.8 ± 0.2	33.6 ± 3.6	33.7 ± 3.5	0.93 ± 0.02
7457	0	1.9 ± 0.2	0.9 ± 0.3	1.1 ± 0.2	0.84 ± 0.05	6.26	2.4 ± 0.3	1.0 ± 0.3	1.2 ± 0.2	0.85 ± 0.05
	0.5		1.1 ± 0.3	1.3 ± 0.3	0.86 ± 0.05		2.4 ± 0.3	1.1 ± 0.3	1.3 ± 0.3	0.87 ± 0.05
	−0.5		0.9 ± 0.2	1.0 ± 0.2	0.83 ± 0.06		2.4 ± 0.3	0.9 ± 0.2	1.1 ± 0.2	0.84 ± 0.05
3607	0	0.3 ± 0.1	2.5 ± 0.7	2.5 ± 0.7	0.3 ± 0.45	20.72	1.3 ± 0.6	10.0 ± 2.4	10.1 ± 2.4	0.81 ± 0.1
	0.5		2.4 ± 0.6	2.4 ± 0.6	0.28 ± 0.6		1.3 ± 0.6	9.6 ± 2.3	9.7 ± 2.4	0.8 ± 0.09
	−0.5		2.5 ± 0.7	2.5 ± 0.7	0.31 ± 0.32		1.3 ± 0.6	10.1 ± 2.4	10.2 ± 2.4	0.81 ± 0.07
5866	0	0.1 ± 0.3	1.2 ± 0.6	1.3 ± 0.5	0.33 ± 0.45	5.75	–	–	–	–
	0.5		1.3 ± 0.6	1.3 ± 0.5	0.35 ± 0.54		–	–	–	–
	−0.5		1.2 ± 0.6	1.2 ± 0.5	0.31 ± 0.61		–	–	–	–

ETGs beyond 5 $R_{\rm e}$ (e.g. Coccato et al. 2009; Pota et al. 2013) with dynamical tracers often showing significant rotation in the outer haloes. Therefore, there is a non-negligible mass contribution from rotation, especially in the flattened ETGs, that needs to be accounted for. We obtain the best-fitting rotation amplitude ($V_{\rm rot}$), velocity dispersion (σ) and kinematic position angle ($PA_{\rm kin}$), respectively, for each galaxy by fitting

$$V_{{\rm mod},i} = V_{\rm sys} \pm \frac{V_{\rm rot}}{\sqrt{1 + \left(\frac{\tan(PA_i - PA_{\rm kin})}{q_{\rm kin}}\right)^2}} \tag{12}$$

to our GC data while we minimize

$$\chi^2 \propto \sum_i \left[\frac{(V_i - V_{{\rm mod},i})^2}{(\sigma^2 + (\Delta V_i)^2)} + \ln(\sigma^2 + (\Delta V_i)^2)\right]. \tag{13}$$

These equations are commonly used in studies of GC kinematics (e.g. Bergond et al. 2006; Pota et al. 2013). In equations (12) and (13), V_i, ΔV_i and $PA_{\rm i}$ are the measured radial velocities, uncertainties on the measured radial velocities and position angles of the GCs, respectively. $V_{\rm sys}$ is the galaxy recession velocity and we fix $q_{\rm kin}$ to the photometric axial ratio q. The uncertainties on the kinematic parameters are obtained through Monte Carlo simulations.

We summarize the significance of rotation by quantifying $V_{\rm rot}/\sigma$ for each GC system. We note that while few ETGs have GC systems that are rotation dominated with $V_{\rm rot}/\sigma > 1$, most of them show significant rotation ($V_{\rm rot}/\sigma \geq 0.4$). We therefore quantify the rotationally supported mass, $M_{\rm rot}$, enclosed within projected radius $R_{\rm out}$ using

$$M_{\rm rot} = \frac{R_{\rm out} {V_{\rm rot}}^2}{G}. \tag{14}$$

Fig. 7 shows the contribution from rotation to the total mass within 5 $R_{\rm e}$. For galaxies in our sample, the average contribution from rotation to the total mass is ∼6 per cent, with the maximum underestimation of ∼20 per cent in NGC 4526 and NGC 4564.

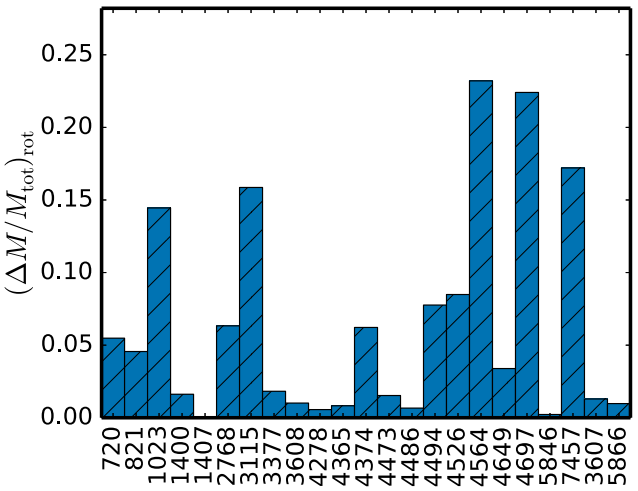

Figure 7. Bar chart showing effect of rotation in the tracer population on the total dynamical mass within 5 $R_{\rm e}$. For our galaxy sample, the average mass underestimation is ∼6 per cent.

3.5 Quantifying the effect of kinematic substructures on mass estimates

For the galaxies with statistically significant kinematic substructures, identified in Section 2.2, we obtain new mass estimates using the *cleaned* catalogues and compare them with the mass estimates from the original catalogues, within 5 $R_{\rm e}$ and under different isotropy assumptions. Fig. 8 shows the fractional change in the mass estimate due to the kinematic substructure $(\Delta M/M_{\rm tot})_{\rm sub}$ for isotropic, radial and tangential velocity distributions. Removing kinematic substructures lead to reduction in mass estimates and

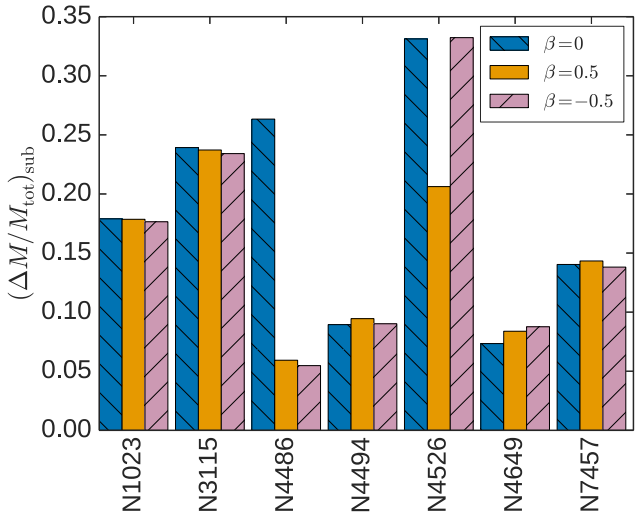

Figure 8. Effect of kinematic substructures on mass estimates within 5 $R_{\rm e}$ for galaxies with statistically significant kinematic substructures. The bar chart shows the fractional mass overestimation due to kinematic substructures. It also shows how the mass estimate changes depending on the assumption made for the orbital anisotropy parameter, β. For our galaxy sample, kinematic substructures lead to ∼14–19 per cent overestimation in total mass, depending on β.

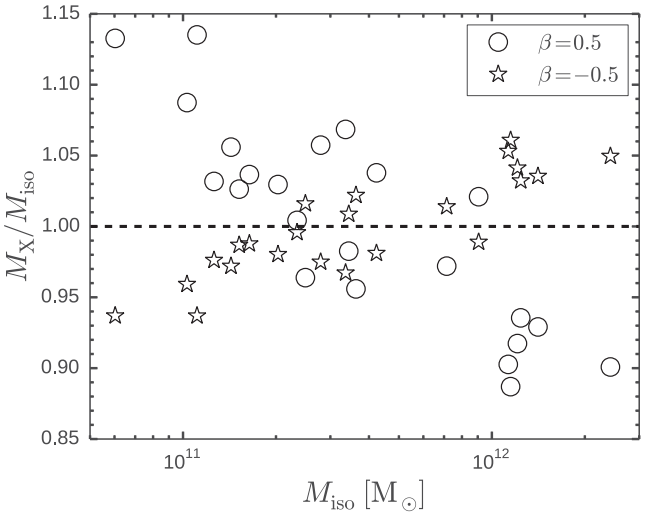

Figure 9. Deviation of mass estimate for radial or tangential anisotropy compared to the isotropic mass estimate. The circles are the mass estimates when orbital anisotropy is radially biased ($\beta = 0.5$), while the stars are mass estimates when tangential anisotropy ($\beta = -0.5$) is assumed. The total mass estimates within 5 $R_{\rm e}$ in most of the galaxies are insensitive to anisotropy, with the average variation of the mass estimates being ≤5 per cent.

for our galaxy sample, the average *overestimation* varies from ∼14 to 19 per cent, depending on velocity anisotropy. This agrees with the study of Yencho et al. (2006) where the effect of substructure on mass estimate of galaxies was found to be ∼20 per cent. The greatest fractional mass overestimation is found in NGC 4526 (∼30 per cent). For the galaxies with identified kinematic substructures, the total mass estimates in Table 3 are from the *cleaned* catalogues, i.e. corrected for substructures.

3.6 Total mass estimates

Table 3 contains a summary of the mass contribution from rotation, $M_{\rm rot}$ and pressure support, $M_{\rm p}$ (corrected for galaxy flattening) for all the galaxies studied in this paper. $M_{\rm p}$ is calculated with $V_{\rm rot}$ subtracted from $V_{\rm los,\,i}$ as prescribed in Evans et al. (2003). We account for the effects of galaxy flattening and rotation in our total dynamical mass estimate, $M_{\rm tot}(<R_{\rm out})$ using

$$M_{\rm tot}(<R_{\rm out}) = {\rm corr} \times M_{\rm p}(<R_{\rm out}) + M_{\rm rot}. \quad (15)$$

Again, we note that for galaxies with identified kinematic substructures, the mass estimates in Table 3 are from the *cleaned* catalogues. For example, in NGC 3115, we account for the mass *overestimation* due to galaxy flattening by applying an ∼15 per cent reduction to $M_{\rm p}$, and it is this corrected value that we show in Table 3.

The mass estimates we list in Table 3 have been obtained assuming $\beta \equiv -0.5, 0, 0.5$. The uncertainty on the total mass varies with the total number of GCs, $N_{\rm GC}$, such that when $N_{\rm GC} \geq 100$ and after accounting for individual $V_{\rm los}$ error via Monte Carlo simulations, the typical uncertainty is ∼0.12 dex. For galaxies with $N_{\rm GC} \sim 70$ and ≤40, typical uncertainties on total mass are ∼0.20 and ∼0.25 dex, respectively.

We show how the total mass estimates, assuming mildly tangential and strong radial anisotropies, deviate from that obtained under isotropy condition in Fig. 9. Mass estimates are largely insensitive to our choice of β: only NGC 3377, NGC 7457 and NGC 1407 show deviations larger than 10 per cent, in agreement with the findings of Bacon (1985). In what follows, we adopt the mass estimates obtained under isotropy conditions, bearing in mind the potential deviations for each galaxy.

3.7 Comparison of mass estimates with results from the literature

In Table 4, we compare mass estimates for our galaxies to the literature. We show the comparison in Fig. 10. The literature sample include studies with PNe, GCs and X-rays as the mass tracers and a variety of generally more sophisticated mass modelling techniques. For example, 9 galaxies from our sample were studied homogeneously by D+12 using PNe and/or GC kinematic data out to 5 $R_{\rm e}$. They did not account for galaxy flattening, rotation of the tracers and kinematic substructures in their mass estimates, even though they modelled the velocity anisotropy. The comparisons are done at the same galactocentric radii (not always at 5 $R_{\rm e}$) as reported in the literature. We have excluded mass estimates from the X-ray study of Churazov et al. (2010) from our comparison since those results are simple power-law fits to their data which underestimates the total mass.

The most deviant results are for NGC 1407 from the X-ray studies of Das et al. (2010) and Su et al. (2014) which both suggest a greater total mass (by a factor of ∼3) compared to what is obtained from GCs. This could be due to their assumption of hydrostatic equilibrium for the Eridanus A group, which may be wrong as the ripples in the X-ray maps (Su et al. 2014) seem to suggest. Mass estimates obtained by studying the phase-space distribution function of tracers (D+12) tend to be systematically lower than those from other methods. This is most likely related to the modelling assumptions made in the study e.g. they restricted $\alpha > 0$. For mass estimates obtained from GC kinematics, the two galaxies with the greatest offsets from our results are NGC 4486 (Murphy et al. 2011) and NGC 4649 (Shen & Gebhardt 2010). The mass overestimation for NGC 4486 has been attributed in the literature to the problematic data used in the study (see Strader et al. 2011; Zhu et al. 2014). For NGC 4649, there is a wide spread in the mass estimates obtained

Table 4. Mass estimates from the literature obtained using different mass tracers and modelling techniques, and comparison with results from this work, obtained assuming $\beta = 0$ and allowing the slope of the gravitational potential to vary with galaxy stellar mass. $M_{\rm lit.}$ and $M_{\rm TME}$ are the total masses from the literature and this work, respectively, within projected radial distance R.

Galaxy (NGC)	R (kpc)	$M_{\rm lit.}$ (10^{11} M$_\odot$)	$M_{\rm TME}$ (10^{11} M$_\odot$)	Tracer
720	20	5.1 ± 0.4	2.8 ± 0.6	X-ray[a]
821	22	2.3 ± 0.6	4.3 ± 0.1	PNe[b]
1023	10	1.7 ± 0.6	1.6 ± 0.3	PNe[c]
1407	68	30.6 ± 3.9	20.9 ± 1.7	GC[d]
	29	9.4 ± 1.3	8.2 ± 0.9	GC[b]
	25	21.6 ± 6.9	7.1 ± 0.7	X-ray[e]
	100	100.0	30.5 ± 2.2	X-ray[f]
2768	14	3.2 ± 1.5	3.7 ± 0.6	PNe[c]
3115	7	1.1 ± 0.5	2.1 ± 0.3	PNe[c]
3377	10	0.7 ± 0.2	0.6 ± 0.1	PNe[b]
4365	15	3.9 ± 0.6	6.2 ± 0.6	X-ray[g]
4374	32	11.5 ± 1.2	17.7 ± 3.9	PNe[s]
	30	15.9 ± 1.9	17.1 ± 3.8	PNe[b]
	29	19.2 ± 1.8	16.5 ± 3.7	PNe[i]
4486	46	33.3 ± 3.3	35.4 ± 2.3	GC[b]
	135	85.2 ± 10.1	97.2 ± 5.4	GC[j]
	180	149.6 ± 20.0	130.6 ± 7.2	GC[i]
	180	191.0 ± 21.0	130.6 ± 7.2	GC[k]
	47	57.0 ± 11.0	36.3 ± 2.3	GC[l]
	120	125.0 ± 7.0	86.7 ± 4.9	X-ray[e]
4494	20	1.6 ± 0.3	1.4 ± 0.2	PNe[m]
	20	1.2 ± 0.2	1.4 ± 0.2	PNe[b]
	19	2.1 ± 0.1	1.3 ± 0.2	PNe[n]
4564	7	0.4 ± 0.1	1.0 ± 0.2	PNe[b]
4649	46	8.7 ± 1.3	19.1 ± 1.3	PNe[b]
	25	16.3 ± 4.3	10.5 ± 0.8	X-ray[e]
	45	34	18.6 ± 1.3	GC[o]
	45	22	18.6 ± 1.3	GC[p]
4697	17	1.4 ± 0.2	8.9 ± 2.2	PNe[b]
	15	1.9 ± 0.3	8.3 ± 2.2	PNe[q]
5846	56	17.0 ± 3.0	19.8 ± 2.1	PNe,GC[r]
	45	16.0 ± 3.3	16.2 ± 1.8	GC[h]
	45	11.2 ± 2.7	16.2 ± 1.8	PNe[b]
	25	12.5 ± 1.9	9.9 ± 1.5	X-ray[e]
7457	5	0.2 ± 0.1	0.6 ± 0.1	PNe[c]
3607	20	3.3 ± 0.7	2.0 ± 0.5	X-ray[g]

References: [a]Humphrey & Buote (2010) and Trujillo-Gomez et al. (2011); [b]Deason et al. (2012); [c]Cortesi et al. (2013); [d]Pota et al. (2015); [e]Das et al. (2010); [f]Su et al. (2014); [g]Nagino & Matsushita (2009) and Trujillo-Gomez et al. (2011); [h]Napolitano et al. (2014); [i]Zhu et al. (2014); [j]Agnello et al. (2014); [k]Oldham & Auger (2016); [l]Murphy, Gebhardt & Adams (2011); [m]Napolitano et al. (2009); [n]Morganti et al. (2013); [o]Shen & Gebhardt (2010); [p]Das et al. (2011); [q]DeLorenzi et al. (2008); [r]Zhu et al. (in preparation); [s]Napolitano et al. (2011).

from GC (Shen & Gebhardt 2010), X-ray (Das et al. 2010) and PN (D+12) data. The GC data used in Shen & Gebhardt (2010) come in part from the catalogue of Lee et al. (2008), in which Pota et al. (2015) identified some extreme velocity objects. This, combined with the kinematic substructures we have identified in this galaxy, could be the source of the differences in the mass estimates for NGC 4649. Another interesting case is NGC 4494, where results using essentially the same data set but different methods give mass estimates that vary by a factor of ∼2.

Lastly, we compare our mass estimates to results from the extended stellar kinematics in the right-hand panel of Fig. 10. Most of the results are from Cappellari et al. (2015, hereafter C+15), where we obtain the total mass by integrating their total mass density profiles. We have also added results from the extended stellar kinematics of Weijmans et al. (2009) and Forestell & Gebhardt (2010) for NGC 821 and the cold-gas study of den Heijer et al. (2015) for NGC 4278. The agreement between our mass estimates and literature mass measurements from stellar kinematics is similar to that in the *right-hand panel* of Fig. 10, though with some individual discrepancies. For example, we find the largest deviation in NGC 821, where our mass estimate differs from that of C+15 by a factor of 4, while being more consistent with the results from Weijmans et al. (2009) and Forestell & Gebhardt (2010). Also, the mass estimate for NGC 4494 from C+15 is a factor of ∼2 higher than what we have found.

From Fig. 10, mass estimates from PNe appear to be systematically lower compared to those from GCs and X-ray data, especially for the more massive galaxies. Our masses also appear to be systematically lower than literature values obtained using GCs. If we assume that all the mass measurements (stars, GCs, PN and X-rays) have comparable errors, then the observed 1σ scatter about the one-to-one relation between the literature values and our mass estimates is 0.3 dex. If we exclude the X-ray data, the scatter is reduced to 0.2 dex. These rms scatters are however upper limits since we only consider total mass estimates obtained assuming isotropy, α varying with stellar mass and stellar $M/L_K = 1$ for the comparison. On a galaxy by galaxy basis, the scatter can be reduced significantly by considering specific combinations of these parameters. Our mass estimates therefore compare well with results from more sophisticated modelling techniques, and from different mass tracers over a wide radial range that extends out to 180 kpc.

3.8 DM fraction

The DM fraction is a useful parameter in understanding the mass distribution as a function of radius in galaxies. We define the DM fraction, $f_{\rm DM}$, as

$$f_{\rm DM}(<R) = 1 - M_*(<R)/M_{\rm tot}(<R), \quad (16)$$

where $M_*(<R)$ and $M_{\rm tot}(<R)$ are the enclosed stellar and total dynamical mass, respectively, within the projected radial distance R. Equation (16) assumes that gas and dust do not contribute significantly to the baryonic mass. The total stellar mass enclosed within R is described by the projected Sérsic mass profile (Sérsic 1968; Terzić & Graham 2005) and it depends on the Sérsic index, n. We use the $R_{\rm e}$–n relation from Graham (2013) to obtain unique Sérsic indices for our galaxies and summarize $f_{\rm DM}$ in Table 3. Similar results are obtained if a luminosity–concentration relation or a de Vaucouleurs' profile ($n = 4$) is assumed for our galaxy sample.

3.9 Total mass and DM fraction beyond 5 $R_{\rm e}$

We extend our mass estimation method to GC kinematic data beyond 5 $R_{\rm e}$ and obtain the total mass and DM fraction enclosed within the maximum probed radius ($R_{\rm max}$). We summarize our results in Table 3, where we have assumed stellar $M/L_K = 1$. NGC 4697 and NGC 5866 have been excluded from this analysis due to the limited radial extent of their GC kinematic data.

To properly understand how the total mass changes with galactocentric radius, we use the method of Napolitano et al. (2005)

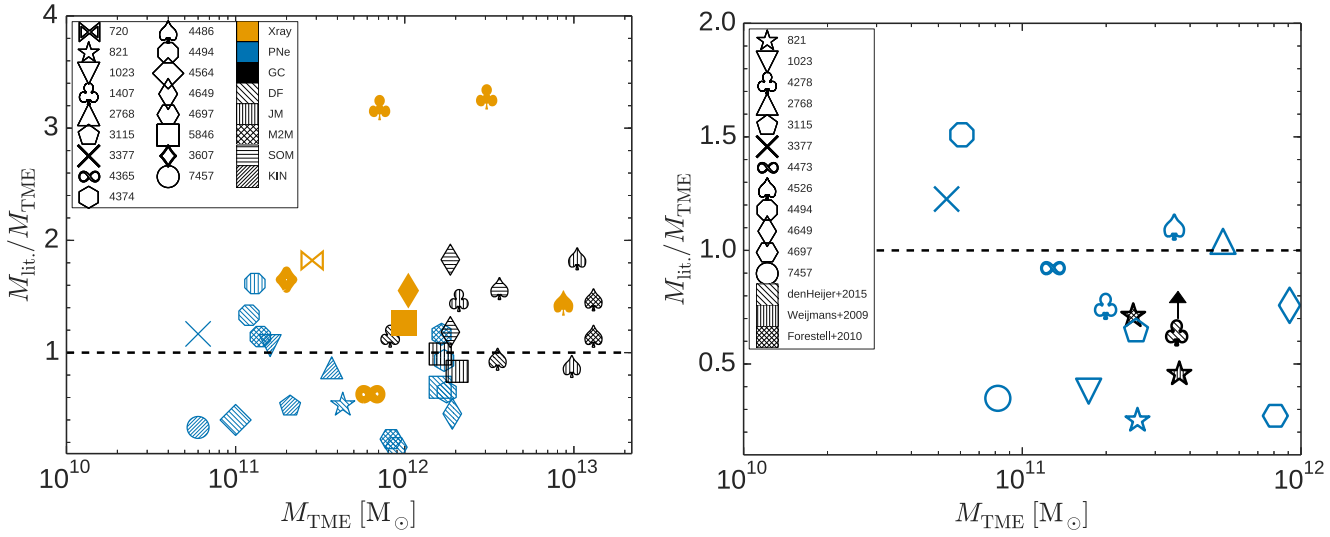

Figure 10. Comparison of mass estimates for galaxies in our sample with results from the literature obtained using different mass tracers and modelling techniques. Left-hand panel: galaxies are identified as shown in the plot legend, with brown, blue and black symbols highlighting the mass tracers used. The hatch marks differentiate galaxies according to the modelling technique employed. DF indicates the phase-space distribution function technique used in D+12, JM is the traditional Jeans mass modelling technique, e.g. Pota et al. (2015), M2M is the made-to-measure mass model, e.g. DeLorenzi et al. (2008), SOM is the Schwarzschild orbit-based modelling technique used in Murphy et al. (2011) while KIN is the asymmetric drift method employed by Cortesi et al. (2013) to extract circular velocities from PNe kinematics, respectively. Right-hand panel: comparison of mass estimates with results from the literature based on extended stellar kinematics. Most of the data points are from the extended stellar kinematics study of Cappellari et al. (2015) which we supplement with results from Weijmans et al. (2009) and Forestell & Gebhardt (2010) for NGC 821. We also include the mass estimate for NGC 4278 from the cold-gas study of den Heijer et al. (2015), assuming their result was measured at 15 kpc (the arrow shows how the mass estimates compare towards 28 kpc). Combining all the data (i.e. PNe, GCs and stars, without the X-ray data) and assuming comparable errors, we observe a 1σ scatter of 0.2 dex between our mass estimates and literature values. This figure is available in colour in the online version.

to obtain the mass-to-light (M/L) gradient between 5 $R_{\rm e}$ and the maximum radius. We use

$$\nabla\Upsilon \equiv \frac{R_{\rm e}}{\Delta R}\left[\left(\frac{M_{\rm DM}}{M_*}\right)_{\rm out} - \left(\frac{M_{\rm DM}}{M_*}\right)_{\rm in}\right], \quad (17)$$

where $\nabla\Upsilon$ is the M/L gradient, $M_{\rm DM}$ and M_* are the enclosed DM and stellar mass, respectively. Fig. 11 shows $\nabla\Upsilon$ versus the total stellar mass of our galaxies. For comparison, we have added data points from Napolitano et al. (2005), where a similar analysis was done using data extending out to $\sim$4 $R_{\rm e}$ (they compiled results from the literature from dynamical studies based on discrete tracers and extended integrated stellar light). The systematic offset between the trend in our data and that of Napolitano et al. (2005) is because we probe radial regions that are more DM dominated (see their Fig. 3). We note that similar results are obtained when $\alpha = 0$ or an outer radius beyond 5 $R_{\rm e}$ is used.

The gradient is shallow for galaxies with stellar mass below $\sim 10^{11.2}$ M$_\odot$, however beyond this transition stellar mass, a sharp upturn in the gradient is observed, with the more luminous galaxies showing a wide variety of gradients. This dichotomy is the direct effect of the difference in the relative radial distribution of stellar mass and DM in ETGs. The transition stellar mass coincides with the upturn in the galaxy M_*–$R_{\rm e}$ relation, such that in the lower mass galaxies, where $R_{\rm e}$ varies slowly with M_*, the scale radius of the DM halo also varies slowly with M_*, hence the flat gradients. For the more massive galaxies, as $R_{\rm e}$ increases rapidly with M_*, we are able to probe more DM.

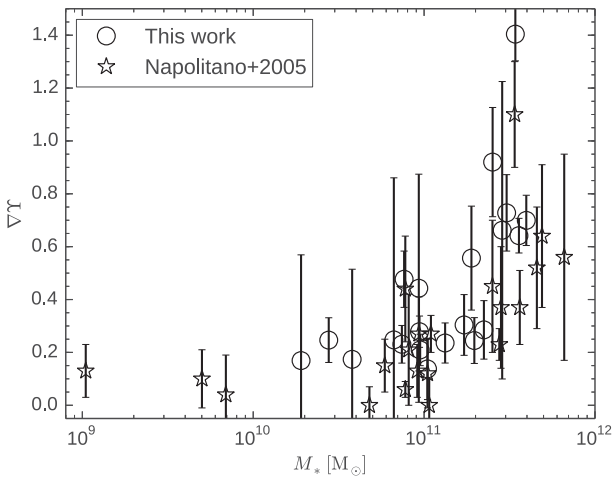

Figure 11. M/L gradient (between 5 $R_{\rm e}$ and the maximum radial limit) versus total stellar mass. The circles are the results from this work, while the stars are from Napolitano et al. (2005). Note that Napolitano et al. (2005) obtained their gradients over the range 0.1–4 $R_{\rm e}$, while the gradients in this work have been obtained between 5 $R_{\rm e}$ and larger radii. The systematic offset between the trend in our data and that of Napolitano et al. (2005) is because we probe radial regions that are more DM dominated (see their Fig. 3). The low and intermediate stellar mass galaxies have shallow total mass gradients and the more massive galaxies show much steeper gradients. NGC 4697 and NGC 5866 are not shown in this plot due to the limited radial extent of their GC kinematic data.

4 DISCUSSION

In the previous section, we homogeneously obtained total mass estimates and DM fraction within 5 $R_{\rm e}$ and beyond, and showed that our mass estimates are consistent with previous studies in the literature, with an observed rms scatter (upper limit) of 0.2 dex. We also used the DM fraction, $f_{\rm DM}$, to describe the relative radial distribution of the stellar and DM in our sample.

4.1 DM fractions and galaxy models

To properly understand these results within the ΛCDM framework, we compare the $f_{\rm DM}$ within 5 $R_{\rm e}$ with predictions from a simple galaxy model where we assume that the DM content follows an NFW profile (Navarro, Frenk & White 1996), with the stellar content described by a Sérsic (1968) mass profile. Starting with the galaxy stellar mass, we use the $R_{\rm e}$–M_* relation from Lange et al. (2015) to obtain model galaxy sizes over our stellar mass range. Next, the non-linear M_*–halo mass relation for ETGs from Dutton et al. (2010) gives the galaxy halo mass, M_{200}, for a given total stellar mass. The halo is then completely parametrized by obtaining the halo concentration parameter, c_{200}, using the M_{200}–c_{200} relation from Dutton & Macciò (2014) based on the *Planck* cosmology. We note that at a fixed halo mass, *Planck* cosmology yields higher halo concentration than the *WMAP5* cosmology, but only slightly alters the $f_{\rm DM}$. We then obtain the scale radius, $r_{\rm s}$, of the galaxy halo using $M_{200} = 4\pi\Delta_{\rm vir}\rho_{\rm cri}{r_{200}}^3/3$ and $r_s \equiv r_{200}/c_{200}$. Armed with the $r_{\rm s}$, c_{200} for any given $R_{\rm e}$–M_* pair plus a universal baryon fraction of 0.17 (Spergel et al. 2007), we then produce the cumulative NFW DM-only radial profiles out to large radii. Likewise, for each $R_{\rm e}$–M_* pair, we use the $R_{\rm e}$–n relation from Graham (2013) and describe the cumulative stellar mass radial profile as defined in Terzić & Graham (2005).

Our total stellar masses have been obtained assuming a global stellar M/L ratio of $M/L_{\rm K} = 1$. This assumption does not reflect differences in the stellar population parameters (e.g. age, metallicity, stellar initial mass function) of ETGs, especially in their central regions. However, we note that our SLUGGS galaxies are generally dominated by very old (8–14 Gyr) stellar populations and have a small range in mean metallicity (McDermid et al. 2015). The $M/L_{\rm K}$ is largely insensitive to metallicity variations (Forbes et al. 2008; Conroy & van Dokkum 2012). For example, fig. 10 from Forbes et al. (2008) shows that the stellar $M/L_{\rm K}$ can vary by ∼0.15 dex within the metallicity range of our sample ($-0.2 \leq$ [Fe/H] ≤ 0.1), which is comparable to the uncertainties on our stellar mass estimates. A similar uncertainty is associated with the observed age variation, i.e. 8–14 Gyr, of our sample.

To test how adopting a stellar $M/L_{\rm K} = 1$ (corresponding to a Kroupa IMF; Kroupa, Tout & Gilmore 1993) may affect our $f_{\rm DM}$, we also obtain $f_{\rm DM}$ using stellar masses from the ATLAS$^{\rm 3D}$ survey. We first use their $(M/L_r)_{\rm Salp}$, obtained from stellar population synthesis models which assumed a Salpeter IMF (table 1, column 5 in Cappellari et al. 2013b) and the galaxy luminosity in the SDSS r band (table 1, column 15 in Cappellari et al. 2013a) to estimate individual stellar masses for the galaxies we have in common. For the four galaxies in our sample that are not in the ATLAS$^{\rm 3D}$ survey, we use the best-fitting function to the K-band magnitude and stellar mass data of their 260 galaxies to infer the stellar masses. We also use their best fit $(M/L_r)_{\rm stars}$ (table 1, column 4 in Cappellari et al. 2013b), obtained from dynamical modelling as total mass minus DM mass, to obtain the stellar mass. This method avoids the potential issue of a non-universal stellar $M/L_{\rm K}$ for our sample when deriving the stellar masses, since recent results suggest that stellar M/L systematically varies with galaxy mass (e.g. Cappellari et al. 2012; Conroy & van Dokkum 2012; Pastorello et al. 2014; Spiniello et al. 2014). On average, these stellar masses are consistent with those listed in Table 2 within ∼0.3 dex.

In Fig. 12, we compare the *predicted* $f_{\rm DM}$ for our galaxy sample with the *measured* $f_{\rm DM}$ within 5 $R_{\rm e}$. The average $f_{\rm DM}$ for our sample is 0.6 ± 0.2, varying from 0.3 in NGC 3607 to 0.9 in NGC 4486. $f_{\rm DM}$ is predicted to increase with galaxy stellar mass while low and high stellar mass galaxies are seen to be DM dominated within 5 $R_{\rm e}$, consistent with the model predictions. However, our $f_{\rm DM}$ measurements reveal discrepancies between predicted and measured $f_{\rm DM}$ for galaxies in the intermediate stellar mass bin ($\sim 10^{11}\,{\rm M}_\odot$). To ascertain if this trend is driven by our stellar $M/L_{\rm K} = 1$ assumption, we repeat the entire analyses, adopting the stellar masses obtained earlier with alternative $M/L_{\rm K}$ assumptions. This is an important exercise, bearing in mind the uncertain contribution from the stellar mass to the total mass estimate. The trend in the measured $f_{\rm DM}$ within 5 $R_{\rm e}$ persists for a variety of stellar M/L assumptions. We note again for clarity that while the results we show in Fig. 12 were obtained under the additional assumption of isotropy, the trends are the same regardless of orbital anisotropies. For some of our galaxies, especially in the intermediate stellar mass bin, the Salpeter IMF (Salpeter 1955) gives stellar mass greater than the total dynamical mass estimate. The tension between predictions and measurements is however reduced when a Kroupa IMF (Kroupa et al. 1993) is assumed. This is not surprising as a Kroupa IMF implies ∼40 per cent less stellar mass compared to a Salpeter IMF. The low- and high-stellar mass galaxies are however consistent with both Salpeter and Kroupa IMF.

We have also checked to see if the corrections we applied for galaxy flattening and inclinations alter our results. We performed our entire analysis assuming that all our galaxies are spherical and observed edge-on, i.e. $q = 1$ and $i = 90$ deg. This implies that in Table 3 and in equations (5) and (15), $q = 1$ and corr $= 1$, respectively. A two-sided KS test of $M_{\rm tot}$ and $f_{\rm DM}$ thus obtained with our earlier results shows that they are identical, i.e. one cannot rule out that they are drawn from the same distribution.

The galaxy model above is simplistic and does not explicitly account for processes which may alter the distribution of DM during galaxy assembly. In Fig. 13, we therefore compare the observed $f_{\rm DM}$ within 5 $R_{\rm e}$ with results from the simulation of W+14, where both the observed and simulated galaxies covered a comparable stellar mass range. In their simulations, they allowed the DM density distribution to be modified during galaxy assembly via processes like adiabatic halo contraction and halo expansion, such that the inner DM density is different from the NFW DM density we adopted in our simple galaxy model. The W+14 simulations however did not account for AGN and/or supernovae feedback processes, therefore, their haloes host galaxies with efficient star formation histories and stellar masses a factor of 2–3 above the expectations from a typical galaxy M_*–halo mass relation. At any given halo mass, their simulations yield significantly lower $f_{\rm DM}$ than our vanilla model predicts, but in better agreement with our measurements for the intermediate mass galaxies with lowered $f_{\rm DM}$. While it is obvious that processes which maximize the stellar mass would result in lower $f_{\rm DM}$, it is however not clear from the simulation if the low $f_{\rm DM}$ is exclusively driven by the baryon–DM interaction or by the feedback processes.

4.2 Total mass and DM fraction, with $\alpha \equiv 0$

In our total mass estimation, we used α derived from the slopes of the circular velocity profiles in the simulation of Wu+14 (see Section 3.2). This allowed α to vary freely between the extremes of Keplerian and logarithmic potentials depending on the galaxy stellar mass. For the most massive galaxies, $\alpha \sim 0$ (see Table 2). However, it is plausible that the low and intermediate stellar mass ETGs reside in isothermal gravitational potential, such that they are better described by $\alpha \equiv 0$. For example, C+15 found $\alpha = 0.27 \pm 0.23$, on 1–4 $R_{\rm e}$ scales for galaxies with a wide range of stellar mass.

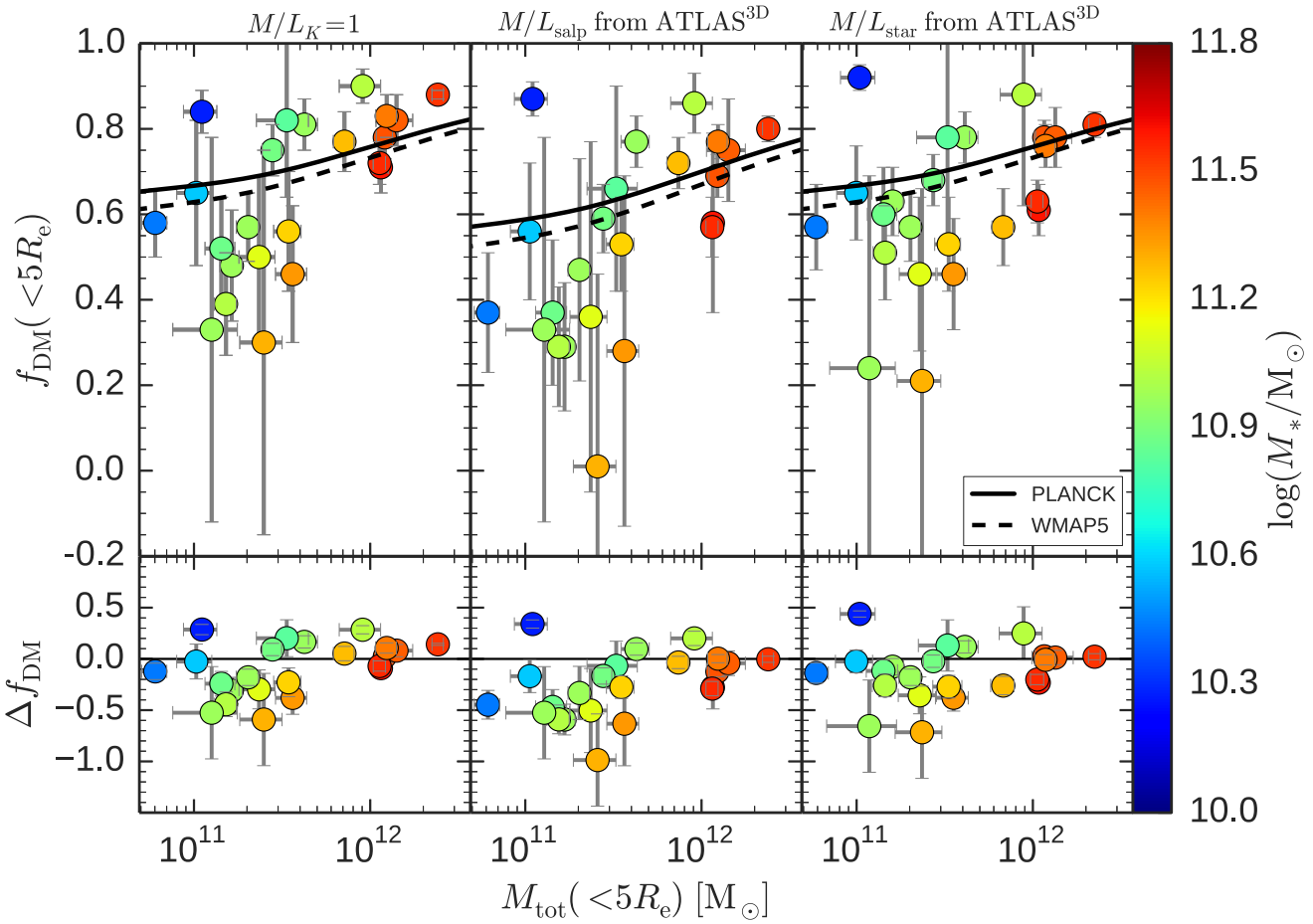

Figure 12. Measured DM fraction, $f_{\rm DM}$, versus the total mass, $M_{\rm tot}$, within 5 effective radii ($R_{\rm e}$). Top panels: in all the top panels, the solid lines show the predicted DM fractions within 5 $R_{\rm e}$ assuming *Planck* cosmology. The dashed lines show the same but assuming *WMAP5* cosmology (see text for details). The marker colour shows the stellar mass of the galaxies. Minimum $f_{\rm DM}$ is observed at stellar mass $\sim 10^{11}$ M$_\odot$. In the left-hand panel, we assume a stellar $M/L_K = 1$, while in the middle and right-hand panels, we use stellar M/L ratios from the ATLAS$^{\rm 3D}$ survey based on a Salpeter IMF and best-fitting stellar M/L ratios from dynamical modelling (total dynamical mass minus DM mass), respectively (Cappellari et al. 2013a,b). Regardless of the adopted stellar M/L ratios, galaxies in the intermediate stellar mass bin have $f_{\rm DM}$ significantly different from what is predicted. Also, low- and high-stellar mass galaxies have higher measured DM fractions than intermediate stellar mass galaxies. Bottom panels: these panels show residuals between predictions (with *Planck* cosmology) and observations, calculated as (observed-predicted)/predicted. This figure is available in colour in the online version.

Also, Thomas et al. (2009) showed that ETGs in the Coma cluster are better described by logarithmic DM haloes rather than NFW DM haloes. This would mean that in our earlier analysis, the total mass and $f_{\rm DM}$ especially for these galaxies would be *underestimated*, depending on how much their α parameter deviates from 0. Since our mass estimator is most sensitive to the α parameter on a galaxy by galaxy basis, it is imperative that we check if the earlier trend we found in the distribution $f_{\rm DM}$ with stellar mass is robust to the value of α.

We therefore re-perform our mass estimation assuming a logarithmic gravitational potential, i.e. $\alpha \equiv 0$, for our sample, and show the result in Fig. 14. The earlier-observed trends in $f_{\rm DM}$ persist, and they are therefore independent of the assumed slope of the gravitational potential, α, as well as the adopted stellar M/L and the orbital anisotropy of the tracers. NGC 3607 has the least $f_{\rm DM}$ within 5 $R_{\rm e}$ in our sample regardless of the adopted stellar M/L ratio. The total mass for NGC 7457 and NGC 4494 are also increased by ∼45 and 35 per cent, respectively. We summarize these mass estimates and $f_{\rm DM}$ in Tables A2 and A4.

4.3 Tension between observations and predictions

The results in Figs 12 and 14 show that the mismatch between observations and predictions of $f_{\rm DM}$ is systematic. Intermediate stellar mass galaxies with $M_* \sim 10^{11}$ M$_\odot$ (NGC 4494, NGC 3607 and NGC 5866) show the greatest deviation from the predicted $f_{\rm DM}$, all with low $f_{\rm DM}$ within 5 $R_{\rm e}$. It is helpful to note that this stellar mass range coincides with the sharp upturn in the galaxy $R_{\rm e}$–M_* relation (e.g. Hyde & Bernardi 2009; Lange et al. 2015) and galaxy peak star formation efficiency (e.g. Shankar et al. 2006; Conroy & Wechsler 2009; Sparre et al. 2015) beyond which halo quenching prevents massive galaxies from accretion of cold gas (e.g. White & Rees 1978; Dutton & Macciò 2014). From our simple galaxy model (see Section 3.8), it is also the stellar mass beyond which $R_{\rm e}/r_{\rm s}$, the ratio of the galaxy size to the scale radius of the DM halo, starts to fall sharply. While the low $f_{\rm DM}$ of these galaxies can be directly linked to a more efficient star formation history, it is interesting to explore why they show more scatter in their $f_{\rm DM}$ compared to ΛCDM predictions. Dutton et al. (2011) showed that intermediate mass galaxies are consistent with Salpeter IMF only when their

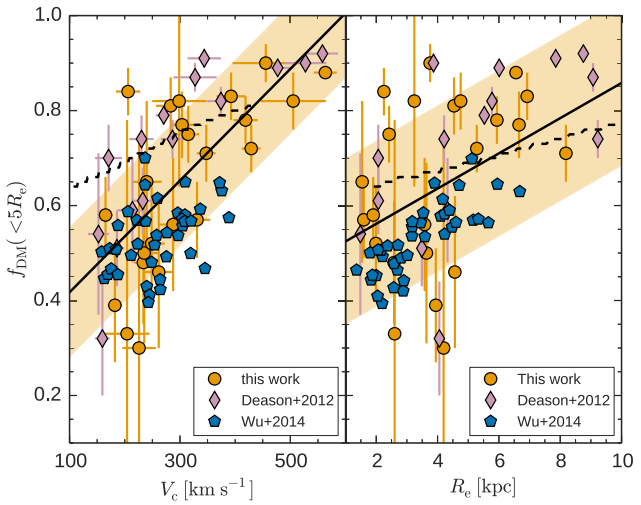

Figure 13. DM fraction within 5 $R_{\rm e}$ versus circular velocity (at 5 $R_{\rm e}$) and galaxy size. Left-hand panel: DM fraction within 5 $R_{\rm e}$ versus circular velocity. Data from our sample, D+12 and from the simulations of Wu+14 are shown as indicated in the plot legend. The best linear fit and intrinsic 1σ scatter to our data are shown by the line and the shaded band, respectively. Right-hand panel: same as in *left-hand panel*, but now showing DM fraction versus galaxy size. Our study, as well as that of D+12 finds a wider range of DM fraction than in the simulations of Wu+14. The simulations yield DM fractions more consistent with the low measurements we have for some of our intermediate mass galaxies. The dashed lines in both panels are from the simple galaxy model with a pristine NFW DM density distribution as discussed in the text.

$V_{\rm c}(R_{\rm e})/\sigma \geq 1.6$. In the top middle panel of Fig. 12, the intermediate mass galaxies that are consistent with a Salpeter IMF are NGC 3608, NGC 821, NGC 4697, NGC 2768 and NGC 4278. We find that these galaxies have $V_{\rm c}(5R_{\rm e})/\sigma \geq 1.3$. NGC 3607, which has the lowest $V_{\rm c}(5R_{\rm e})/\sigma \sim 0.9$, has a negative $f_{\rm DM}$ when a Salpeter IMF is assumed. A simple experiment in which we vary the stellar M/L_K ratio (a proxy for the IMF) reveals that the maximum stellar M/L_K that gives positive $f_{\rm DM}$ for all the galaxies in our sample is ∼1.4. This is shallower than the Salpeter IMF, but steeper than a Kroupa/Chabrier IMF (at a fixed age and metallicity).

One of the intermediate mass galaxies studied here, NGC 4494, has been notoriously difficult to model in the literature, with results ranging from a low DM content (Romanowsky et al. 2003; Napolitano et al. 2009; D+12) to a high DM content (Morganti et al. 2013). Here, using GC kinematic data that extend far out into the halo, we find that NGC 4494 is DM poor, i.e. $f_{\rm DM} \leq 0.5$ at $R_{\rm max} \sim 9\,R_{\rm e}$ regardless of the adopted stellar $M/L_{\rm K}$ and the GC orbital anisotropy when α, the slope of the gravitational potential, is assumed to be 0.2. Our $R_{\rm max}$ for NGC 4494 is close to the scale radius of the NFW DM halo, where the mass distribution is expected to be DM dominated, such that in a typical 10^{13} M$_\odot$ halo, $f_{\rm DM} \sim 0.9$ at the scale radius. However, when $\alpha \equiv 0$ in equation (6), we obtain $f_{\rm DM} \sim 0.3$–0.6 within 5 $R_{\rm e}$ and $f_{\rm DM} \sim 0.5$–0.7 within $R_{\rm max}$, for varying stellar $M/L_{\rm K}$. This is similar to the result from Morganti et al. (2013), obtained also by assuming a logarithmic DM halo. A more detailed dynamical mass modelling of NGC 4494 that combines the existing literature data and the GC data we have studied here would be desirable. Such a study should explore a wide suite of gravitational potentials, galaxy shapes and orbital distributions while incorporating stellar population models.

Galaxies with marginally low $f_{\rm DM}$ within 5 $R_{\rm e}$ e.g. NGC 720, NGC 4526 and NGC 1023, they can be seen to rapidly increase their $f_{\rm DM}$ between 5 $R_{\rm e}$ and their respective $R_{\rm max}$, showing that they are DM dominated. Our study also includes the two most dominant members of the Leo II group (NGC 3607 and NGC 3608) with intriguing $f_{\rm DM}$ measurements. The most luminous member of the group, NGC 3607 ($M_{\rm K} = -24.96$) has $f_{\rm DM} \sim 0.3$ within 5 $R_{\rm e}$. NGC 3607 has the lowest $f_{\rm DM}$ within 5 $R_{\rm e}$ in our sample even when the DM content is maximized with a logarithmic potential, regardless of the adopted stellar $M/L_{\rm K}$. However, beyond 5 $R_{\rm e}$, the $f_{\rm DM}$ in NGC 3607 increases steeply up to ∼0.8, again showing that the outer halo is dominated by DM. The next most luminous member of the group with $M_{\rm K} = -23.78$, NGC 3608, however, has a higher $f_{\rm DM}$ of ∼0.8 within 5 $R_{\rm e}$. Within 5 $R_{\rm e}$, NGC 3607 has an average DM density of $\log\langle\rho_{\rm DM}\rangle \sim 6.2$ M$_\odot$ kpc^{-3}, the lowest in our sample, unlike NGC 3608 with a denser DM halo with $\log\langle\rho_{\rm DM}\rangle \sim 7.2$ M$_\odot$ kpc^{-3}. This suggests that both galaxies have DM haloes that are structurally different, with implications for their assembly time, such that the galaxy with the denser DM halo assembled earlier (Navarro et al. 1996; Bullock et al. 2001; Thomas et al. 2009). As a group, the intermediate stellar mass galaxies with low $f_{\rm DM}$ in our galaxy sample also have the lowest average DM densities. This mirrors the results from Romanowsky et al. (2003) and Napolitano et al. (2005, 2009) where some discy, fast rotating, intermediate stellar mass galaxies showed more diffuse DM haloes than expected. A more detailed investigation of the structural parameters of the DM haloes (with adiabatic halo contraction) is however beyond the scope of this paper.

4.4 Correlations between DM fraction and galaxy properties

In this section, we look for trends in $f_{\rm DM}$ as a function of other galaxy properties. Fig. 15 shows how the measured $f_{\rm DM}$ within 5 $R_{\rm e}$ varies with galaxy ellipticity, central velocity dispersion, galaxy size and galaxy rotation dominance parameter, and we also highlight the environment and morphology of the galaxies (see Table 2). The rotational dominance parameters are from Arnold et al. (2011). Table 5 shows the Spearman rank correlation coefficient and statistical significance of the correlation between the $f_{\rm DM}$ and galaxy properties. The correlations are generally weak, mainly due to the huge scatter introduced by the intermediate stellar mass galaxies identified and discussed in Section 4.3. There is a visible trend in $f_{\rm DM}$ with ϵ. Here, we find that $f_{\rm DM}$ within 5 $R_{\rm e}$ decreases with ϵ. However, there are notable outliers to this trend. The trends with $R_{\rm e}$, σ and V/σ are weak. While the slow rotators in our sample generally have high $f_{\rm DM}$, there is no clear pattern in the fast rotators. The S0 galaxies, however, show a decreasing $f_{\rm DM}$ with σ and $R_{\rm e}$. We do not see any strong trend as a function of environment or morphology. In Fig. 16, we show how $\nabla\Upsilon$ varies with galaxy properties. The correlations are now stronger and statistically significant (see Table 5). The gradients are shallower for flattened galaxies, with the more spherical galaxies showing a great variety of $\nabla\Upsilon$. Larger and more massive galaxies have steeper $\nabla\Upsilon$. There is no clear trend with galaxy environment. However, when the different galaxy morphologies are highlighted, the S0 galaxies are seen to have shallow $\nabla\Upsilon$ regardless of galaxy ellipticity, size, total mass or rotational dominance parameter (the same trend is also evident from the result in Napolitano et al. 2005). The net effect for massive S0 galaxies is to reduce their $R_{\rm e}/r_{\rm s}$ compared to similar stellar mass ellipticals, hence their flattened gradients, i.e. lower $\nabla\Upsilon$.

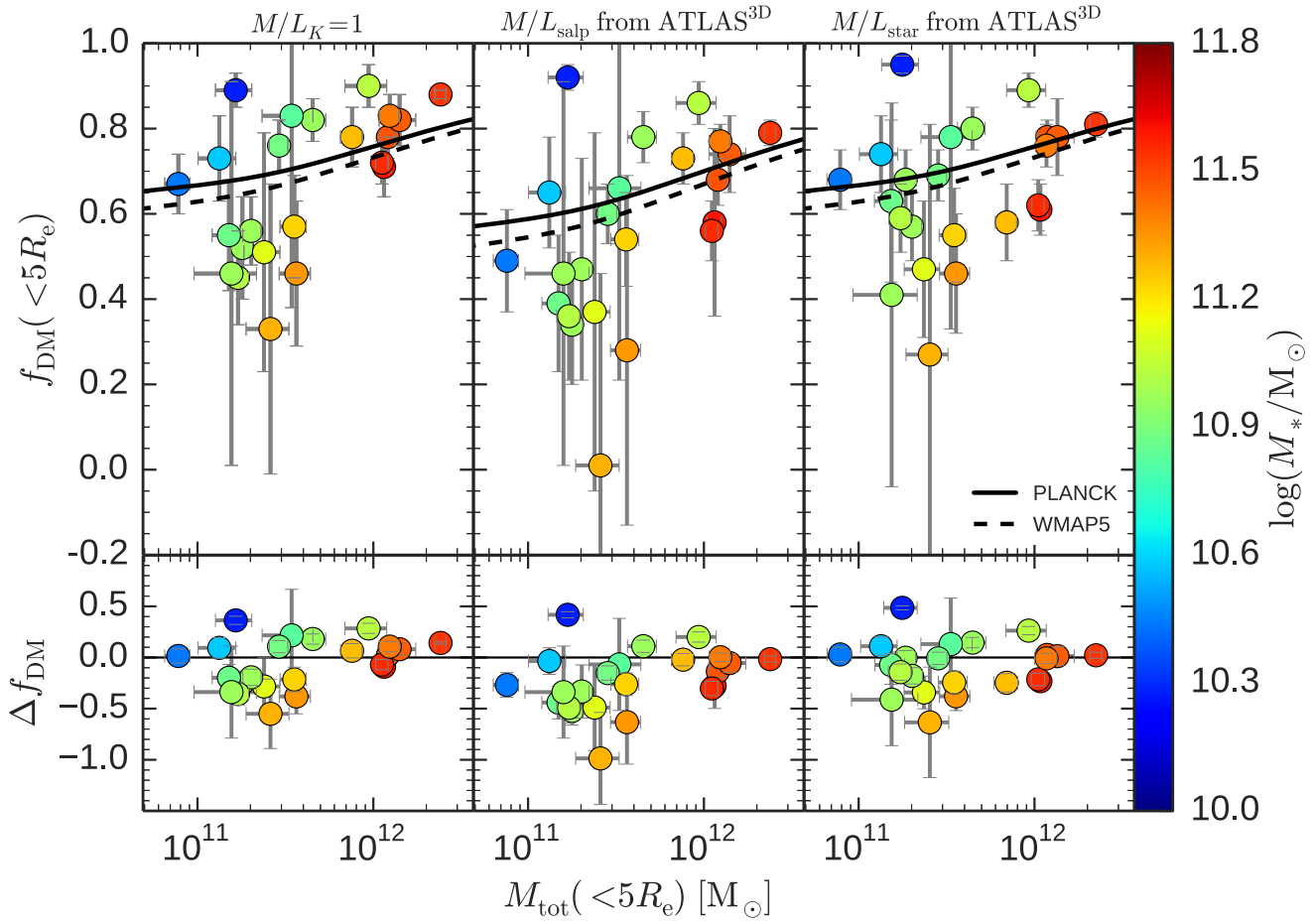

Figure 14. Same as in Fig. 12, but assuming a logarithmic potential for our sample, i.e. $\alpha \equiv 0$ in equation (6). The intermediate stellar mass galaxies still have the lowest $f_{\rm DM}$ in our sample, same as in Fig. 12. This figure is available in colour in the online version.

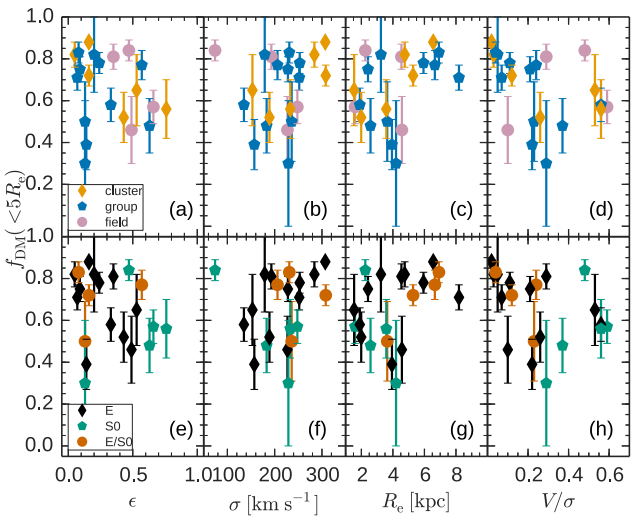

Figure 15. DM fraction within 5 $R_{\rm e}$ versus galaxy parameters. Top panels are colour-coded according to galaxy environment as shown in panel (a) and the bottom panels according to galaxy morphology as shown in panel (e). (Panels a, e) galaxy ellipticity – ϵ, (panels b, f) central velocity dispersion, (panel c, g) effective radius and (panels d, h) rotation dominance parameter. There is no clear trend either as a function of galaxy morphology or environment and the trends with galaxy properties are generally weak.

Table 5. Spearman correlation test and statistical significance of the correlation between the $f_{\rm DM}$ and $\nabla\Upsilon$ and galaxy properties.

Parameters	coeff	p-val	Parameters	coeff	p-val
$f_{\rm DM}-\epsilon$	−0.22	0.32	$\nabla\Upsilon-\epsilon$	−0.37	0.09
$f_{\rm DM}-\sigma$	0.18	0.44	$\nabla\Upsilon-\sigma$	0.76	0.001
$f_{\rm DM}-R_{\rm e}$	0.32	0.16	$\nabla\Upsilon-R_{\rm e}$	0.75	0.001
$f_{\rm DM}-V/\sigma$	−0.44	0.04	$\nabla\Upsilon-V/\sigma$	−0.63	0.001

5 CONCLUSIONS

We have employed a TME to homogeneously obtain mass estimates of 23 ETGs out to 5 $R_{\rm e}$ and beyond, using their GC kinematic data. The galaxies we have studied cover a wide range of total galaxy stellar mass and include galaxies from the field, group and cluster environments. The GC kinematic data have been obtained using the Keck/DEIMOS multi-object spectrograph as part of the SLUGGS survey. We accounted for kinematic substructures, galaxy flattening and rotation in the GC system in our mass estimates. We have done an extensive comparison of our mass estimates with results from the literature obtained using various mass tracers and more sophisticated modelling techniques.

From the mass profiles, we have obtained the DM fraction enclosed within 5 $R_{\rm e}$ and compared our results with predictions from a simple galaxy model (NFW profile for DM plus Sérsic mass profile for the stars). We have also studied the effect of varying the stellar

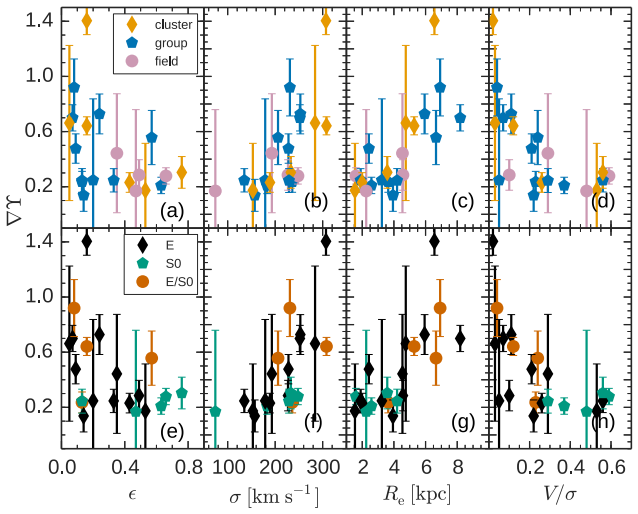

Figure 16. M/L gradient, $\nabla\Upsilon$, versus galaxy parameters. Colour coding is same as in Fig. 15. (Panels a, e) $\nabla\Upsilon$ versus galaxy ellipticity – ϵ, (panels b, f) $\nabla\Upsilon$ versus central velocity dispersion, (panels c, g) $\nabla\Upsilon$ versus effective radius and (panels d, h) $\nabla\Upsilon$ versus rotation dominance parameter. Galaxies with $\epsilon \sim 0$, large σ and larger R_e have steeper gradients. An interesting trend is seen in panel h where the S0 galaxies have shallow $\nabla\Upsilon$ regardless of galaxy ellipticity, size or mass.

M/L ratio (consistent with either a Salpeter or a Kroupa-like IMF or one that varies with galaxy stellar mass) on our results. Since our GC data extend well beyond 5 R_e, we have quantified the gradient of the DM fraction between 5 R_e and the maximum probed radius. Lastly, we studied trends in the DM fraction as a function of galaxy properties.

The salient results are as follows.

(i) Mass estimates obtained using GC kinematic data and the TME are consistent with those obtained from more sophisticated modelling techniques and with various mass tracers over a radial range that extends out to $\sim$13 R_e. Using the TME, we are able to obtain mass estimates out to $\sim$10 R_e in low-mass galaxies with relatively sparse dynamical tracers. We find an upper limit of 0.2 dex in the observed 1σ scatter around the one-to-one comparison line between our mass estimates and those from the literature.

(ii) On average in our sample, kinematic substructures in GC systems leads to mass overestimation by $\sim$19 per cent. Not accounting for GC system rotation leads to mass underestimation by $\sim$6 per cent, while galaxy flattening is responsible for an $\sim$5 per cent mass overestimation with the caveat that our galaxies are mostly edge-on.

(iii) By comparing the total mass enclosed within 5 R_e under various assumptions of velocity anisotropy, we are able to establish that total mass estimates are largely insensitive to GC orbital anisotropy. Only NGC 3377, NGC 7457 and NGC 1407 show mass deviations greater than 10 per cent when mildly tangential or radial anisotropies are assumed rather than isotropy conditions.

(iv) The DM fraction within 5 R_e, f_{DM}, generally increases with galaxy stellar mass. It increases from $f_{DM} \sim 0.6$ in low mass ETGs to $f_{DM} \sim 0.8$ in high-mass ETGs, in line with ΛCDM predictions. However, some intermediate mass galaxies ($\sim 10^{11}$ M$_\odot$), i.e. NGC 4494, NGC 3607 and NGC 5866, have f_{DM} that are significantly lower than what a vanilla galaxy model would predict. This is independent of the assumed stellar M/L_K ratio, the orbital anisotropy of the mass tracers or the shape of the gravitational potential. These lower f_{DM} measurements are consistent with results from the cosmological simulations of Wu+14 where the pristine DM density distribution has been modified via baryon–DM interactions during galaxy assembly. The widely reported dearth of DM in the outer halo of NGC 4494 is alleviated by assuming a logarithmic gravitational potential.

(v) Using total mass estimates within 5 R_e and larger radii (usually comparable to the scale radii of the DM haloes), low and intermediate stellar mass galaxies in our sample have shallow M/L gradients, with the more massive galaxies generally having steeper gradients. This reflects the relative difference in the radial scale of baryons and DM in ETGs. However, lenticular galaxies, regardless of galaxy stellar mass, ellipticity, size and rotational dominance parameter, have shallow gradients.

(vi) We find hints that intermediate stellar mass galaxies with low DM fractions have halo structural parameters that are not typical, i.e. they possess very diffuse DM haloes and they assembled late. This result is interesting and calls for a systematic study of the structural parameters of the haloes of ETGs.

ACKNOWLEDGEMENTS

We wish to thank the anonymous referee for the useful feedback. The data presented herein were obtained at the W.M. Keck Observatory, which is operated as a scientific partnership among the California Institute of Technology, the University of California and the National Aeronautics and Space Administration. The Observatory was made possible by the generous financial support of the W.M. Keck Foundation. The authors wish to recognize and acknowledge the very significant cultural role and reverence that the summit of Mauna Kea has always had within the indigenous Hawaiian community. The analysis pipeline used to reduce the DEIMOS data was developed at UC Berkeley with support from NSF grant AST-0071048. JPB acknowledges support from NSF grant AST-1211995. DAF and JJ thank the ARC for financial support via DP 130100388. We thank Cappellari M. for making his mass profiles available. This research made use of TOPCAT (Taylor 2005) and HYPER.FIT (Robotham & Obreschkow 2015).

REFERENCES

Agnello A., Evans N. W., Romanowsky A. J., Brodie J. P., 2014, MNRAS, 442, 3299
An J. H., Evans N. W., 2011, MNRAS, 413, 1744
Arnold J. A., Romanowsky A. J., Brodie J. P., Chomiuk L., Spitler L. R., Strader J., Benson A. J., Forbes D. A., 2011, ApJ, 736, L26
Arnold J. A. et al., 2014, ApJ, 791, 80
Ashman K. M., Bird C. M., 1993, AJ, 106, 2281
Auger M. W., Treu T., Bolton A. S., Gavazzi R., Koopmans L. V. E., Marshall P. J., Moustakas L. A., Burles S., 2010, ApJ, 724, 511
Bacon R., 1985, A&A, 143, 84
Bahcall J. N., Tremaine S., 1981, ApJ, 244, 805
Barnabè M., Czoske O., Koopmans L. V. E., Treu T., Bolton A. S., 2011, MNRAS, 415, 2215
Bassino L. P., Richtler T., Dirsch B., 2006, MNRAS, 367, 156
Bekki K., Forbes D. A., 2006, A&A, 445, 485
Bender R., Saglia R. P., Gerhard O. E., 1994, MNRAS, 269, 785
Bergond G., Zepf S. E., Romanowsky A. J., Sharples R. M., Rhode K. L., 2006, A&A, 448, 155
Binney J., Mamon G. A., 1982, MNRAS, 200, 361
Binney J., Tremaine S., 1987, Galactic Dynamics. Princeton Univ. Press, Princeton, NJ
Blakeslee J. P. et al., 2009, ApJ, 694, 556
Brodie J. P. et al., 2014, ApJ, 796, 52
Bullock J. S., Johnston K. V., 2005, ApJ, 635, 931

Bullock J. S., Kolatt T. S., Sigad Y., Somerville R. S., Kravtsov A. V., Klypin A. A., Primack J. R., Dekel A., 2001, MNRAS, 321, 559
Cappellari M. et al., 2007, MNRAS, 379, 418
Cappellari M. et al., 2012, Nature, 484, 485
Cappellari M. et al., 2013a, MNRAS, 432, 1709
Cappellari M. et al., 2013b, MNRAS, 432, 1862
Cappellari M. et al., 2015, ApJ, 804, L21 (C+15)
Churazov E. et al., 2010, MNRAS, 404, 1165
Coccato L. et al., 2009, MNRAS, 394, 1249
Conroy C., van Dokkum P. G., 2012, ApJ, 760, 71
Conroy C., Wechsler R. H., 2009, ApJ, 696, 620
Cooper M. C., Newman J. A., Davis M., Finkbeiner D. P., Gerke B. F., 2012, Astrophysics Source Code Library, record ascl:1203.003
Cooper A. P., D'Souza R., Kauffmann G., Wang J., Boylan-Kolchin M., Guo Q., Frenk C. S., White S. D. M., 2013, MNRAS, 434, 3348
Cortesi A. et al., 2013, MNRAS, 432, 1010
Das P., Gerhard O., Churazov E., Zhuravleva I., 2010, MNRAS, 409, 1362
Das P., Gerhard O., Mendez R. H., Teodorescu A. M., de Lorenzi F., 2011, MNRAS, 415, 1244
Deason A. J., Belokurov V., Evans N. W., McCarthy I. G., 2012, ApJ, 748, 2 (D+12)
Dekel A., Stoehr F., Mamon G. A., Cox T. J., Novak G. S., Primack J. R., 2005, Nature, 437, 707
DeLorenzi F., Gerhard O., Saglia R. P., Sambhus N., Debattista V. P., Pannella M., Méndez R. H., 2008, MNRAS, 385, 1729
den Heijer M. et al., 2015, A&A, 581, A98
Di Cintio A., Knebe A., Libeskind N. I., Hoffman Y., Yepes G., Gottlöber S., 2012, MNRAS, 423, 1883
Dirsch B., Schuberth Y., Richtler T., 2005, A&A, 433, 43
Dressler A., Shectman S. A., 1988, AJ, 95, 985
Dutton A. A., Macciò A. V., 2014, MNRAS, 441, 3359
Dutton A. A., Conroy C., van den Bosch F. C., Prada F., More S., 2010, MNRAS, 407, 2
Dutton A. A. et al., 2011, MNRAS, 416, 322
Dutton A. A., Macciò A. V., Mendel J. T., Simard L., 2013, MNRAS, 432, 2496
Einasto M. et al., 2012, A&A, 540, A123
Evans N. W., 1994, MNRAS, 267, 333
Evans N. W., Wilkinson M. I., Perrett K. M., Bridges T. J., 2003, ApJ, 583, 752
Faber S. M. et al., 2003, in Iye M., Moorwood A. F. M., eds, Proc. SPIE Conf. Ser. Vol. 4841, Instrument Design and Performance for Optical/Infrared Ground-based Telescopes. SPIE, Bellingham, p. 1657
Faifer F. R. et al., 2011, MNRAS, 416, 155
Forbes D. A., Lasky P., Graham A. W., Spitler L., 2008, MNRAS, 389, 1924
Forestell A. D., Gebhardt K., 2010, ApJ, 716, 370
Gerhard O., Kronawitter A., Saglia R. P., Bender R., 2001, AJ, 121, 1936
Graham A. W., 2013, in Oswalt T. D., Keel W. C., eds, Planets, Stars and Stellar Systems. Springer Science+Business Media, Dordrecht, p. 91
Harris W. E., 1976, AJ, 81, 1095
Harris W. E., 1986, AJ, 91, 822
Heisler J., Tremaine S., Bahcall J. N., 1985, ApJ, 298, 8
Helmi A., 2008, A&AR, 15, 145
Humphrey P. J., Buote D. A., 2010, MNRAS, 403, 2143
Hyde J. B., Bernardi M., 2009, MNRAS, 394, 1978
Jarrett T. H., Chester T., Cutri R., Schneider S., Skrutskie M., Huchra J. P., 2000, AJ, 119, 2498
Kissler-Patig M., 1997, A&A, 319, 83
Krajnović D., Emsellem E., Cappellari M., Alatalo K., Blitz L., Bois M., Bournaud F., Bureau, 2011, MNRAS, 414, 2923
Kroupa P., Tout C. A., Gilmore G., 1993, MNRAS, 262, 545
Lange R. et al., 2015, MNRAS, 447, 2603
Lee M. G. et al., 2008, ApJ, 674, 857
Limber D. N., Mathews W. G., 1960, ApJ, 132, 286
McDermid R. M. et al., 2015, MNRAS, 448, 3484
Magorrian J., Ballantyne D., 2001, MNRAS, 322, 702
Mendel J. T., Proctor R. N., Forbes D. A., Brough S., 2008, MNRAS, 389, 749
Merrett H. R. et al., 2003, MNRAS, 346, L62
Morganti L., Gerhard O., Coccato L., Martinez-Valpuesta I., Arnaboldi M., 2013, MNRAS, 431, 3570
Murphy J. D., Gebhardt K., Adams J. J., 2011, ApJ, 729, 129
Nagino R., Matsushita K., 2009, A&A, 501, 157
Napolitano N. R. et al., 2005, MNRAS, 357, 691
Napolitano N. R. et al., 2009, MNRAS, 393, 329
Napolitano N. R. et al., 2011, MNRAS, 411, 2035
Napolitano N. R., Pota V., Romanowsky A. J., Forbes D. A., Brodie J. P., Foster C., 2014, MNRAS, 439, 659
Navarro J. F., Frenk C. S., White S. D. M., 1996, ApJ, 462, 563
Okoń W. M. M., Harris W. E., 2002, ApJ, 567, 294
Oldham L. J., Auger M. W., 2016, MNRAS, 457, 421
Oser L., Ostriker J. P., Naab T., Johansson P. H., Burkert A., 2010, ApJ, 725, 2312
Oser L., Naab T., Ostriker J. P., Johansson P. H., 2012, ApJ, 744, 63
Pastorello N., Forbes D. A., Foster C., Brodie J. P., Usher C., Romanowsky A. J., Strader J., Arnold J. A., 2014, MNRAS, 442, 1003
Pinkney J., Roettiger K., Burns J. O., Bird C. M., 1996, ApJS, 104, 1
Pota V. et al., 2013, MNRAS, 428, 389
Pota V. et al., 2015, MNRAS, 450, 1962
Puzia T. H. et al., 2004, A&A, 415, 123
Remus R.-S., Burkert A., Dolag K., Johansson P. H., Naab T., Oser L., Thomas J., 2013, ApJ, 766, 71
Rhode K. L., Zepf S. E., Kundu A., Larner A. N., 2007, AJ, 134, 1403
Robotham A. S. G., Obreschkow D., 2015, PASA, 32, e033
Romanowsky A. J., Douglas N. G., Arnaboldi M., Kuijken K., Merrifield M. R., Napolitano N. R., Capaccioli M., Freeman K. C., 2003, Science, 301, 1696
Romanowsky A. J., Strader J., Brodie J. P., Mihos J. C., Spitler L. R., Forbes D. A., Foster C., Arnold J. A., 2012, ApJ, 748, 29
Salpeter E. E., 1955, ApJ, 121, 161
Schlegel D. J., Finkbeiner D. P., Davis M., 1998, ApJ, 500, 525
Schwarzschild M., 1954, AJ, 59, 273
Scott N., Graham A. W., Schombert J., 2013, ApJ, 768, 76
Sérsic J. L., 1968, Atlas de galaxias australes. Observatorio Astronomico, Cordoba
Shankar F., Lapi A., Salucci P., De Zotti G., Danese L., 2006, ApJ, 643, 14
Shen J., Gebhardt K., 2010, ApJ, 711, 484
Sikkema G., Peletier R. F., Carter D., Valentijn E. A., Balcells M., 2006, A&A, 458, 53
Sparre M. et al., 2015, MNRAS, 447, 3548
Spergel D. N. et al., 2007, ApJS, 170, 377
Spiniello C., Trager S., Koopmans L. V. E., Conroy C., 2014, MNRAS, 438, 1483
Strader J. et al., 2011, ApJS, 197, 33
Su Y., Gu L., White R. E., III, Irwin J., 2014, ApJ, 786, 152
Taylor M. B., 2005, in Shopbell P., Britton M., Ebert R., eds, ASP Conf. Ser. Vol. 347, Astronomical Data Analysis Software and Systems XIV. Astron. Soc. Pac., San Francisco, p. 29
Terzić B., Graham A. W., 2005, MNRAS, 362, 197
Thomas J., Saglia R. P., Bender R., Thomas D., Gebhardt K., Magorrian J., Corsini E. M., Wegner G., 2009, ApJ, 691, 770
Thomas J. et al., 2011, MNRAS, 415, 545
Tonry J. L., Dressler A., Blakeslee J. P., Ajhar E. A., Fletcher A. B., Luppino G. A., Metzger M. R., Moore C. B., 2001, ApJ, 546, 681
Tortora C., La Barbera F., Napolitano N. R., Romanowsky A. J., Ferreras I., de Carvalho R. R., 2014, MNRAS, 445, 115
Trujillo-Gomez S., Klypin A., Primack J., Romanowsky A. J., 2011, ApJ, 742, 16
Watkins L. L., Evans N. W., An J. H., 2010, MNRAS, 406, 264 (W+10)
Watkins L. L., van de Ven G., den Brok M., van den Bosch R. C. E., 2013, MNRAS, 436, 2598
Weijmans A.-M. et al., 2009, MNRAS, 398, 561
White S. D. M., Rees M. J., 1978, MNRAS, 183, 341
Wolf J., Martinez G. D., Bullock J. S., Kaplinghat M., Geha M., Muñoz R. R., Simon J. D., Avedo F. F., 2010, MNRAS, 406, 1220

Wu X., Gerhard O., Naab T., Oser L., Martinez-Valpuesta I., Hilz M., Churazov E., Lyskova N., 2014, MNRAS, 438, 2701 (Wu+14)
Yencho B. M., Johnston K. V., Bullock J. S., Rhode K. L., 2006, ApJ, 643, 154
Zhu L. et al., 2014, ApJ, 792, 59
Zwicky F., 1937, ApJ, 86, 217

APPENDIX A: MASS ESTIMATES AT 8 R_e

Table A1. Mass estimates and DM fraction (f_{DM}) within 8 R_e assuming isotropy. Columns 2–4 show the rotationally supported, pressure-supported (obtained without subtracting V_{rot} from V_{los}) and total dynamical mass within 8 R_e, respectively.

Galaxy (NGC)	$M_{rot}(<8\,R_e)$ ($10^{10}\,M_\odot$)	$M'_p(<8\,R_e)$ ($10^{11}\,M_\odot$)	$M_{tot}(<8\,R_e)$ ($10^{11}\,M_\odot$)	$f_{DM}(<8\,R_e)$
720	3.2 ± 2.0	5.7 ± 1.2	6.0 ± 0.6	0.65 ± 0.06
821	3.2 ± 1.8	5.5 ± 1.0	5.8 ± 0.6	0.85 ± 0.01
1023	3.8 ± 1.1	2.1 ± 0.4	2.4 ± 0.2	0.63 ± 0.02
1407	0.1 ± 0.3	20.0 ± 1.6	20.0 ± 0.9	0.82 ± 0.01
2768	7.2 ± 2.4	9.8 ± 1.6	10.5 ± 0.8	0.83 ± 0.01
3115	5.2 ± 0.9	1.6 ± 0.3	2.1 ± 0.2	0.56 ± 0.02
3377	0.2 ± 0.1	0.8 ± 0.1	0.9 ± 0.1	0.69 ± 0.02
3608	0.6 ± 0.6	3.7 ± 1.1	3.7 ± 0.6	0.83 ± 0.02
4278	0.3 ± 0.2	4.3 ± 0.4	4.4 ± 0.3	0.83 ± 0.01
4365	1.6 ± 1.1	17.0 ± 1.6	17.2 ± 0.9	0.84 ± 0.01
4374	14.0 ± 8.8	22.0 ± 5.2	23.4 ± 3.1	0.89 ± 0.01
4473	0.4 ± 0.3	2.0 ± 0.3	2.0 ± 0.2	0.64 ± 0.02
4486	2.6 ± 1.2	32.4 ± 2.1	32.7 ± 1.2	0.90 ± 0.01
4494	1.9 ± 0.5	1.3 ± 0.2	1.5 ± 0.1	0.34 ± 0.04
4526	4.7 ± 1.9	3.0 ± 0.5	3.5 ± 0.3	0.54 ± 0.03
4649	6.1 ± 1.5	15.5 ± 1.1	16.1 ± 0.7	0.79 ± 0.01
3607	0.5 ± 0.6	5.4 ± 1.4	5.5 ± 0.8	0.66 ± 0.03

Table A2. Mass estimates (M_{tot}) and DM fractions (f_{DM}) within 5 R_e (columns 3 and 4) and R_{max} (columns 5 and 6), respectively, assuming different anisotropy, but with $\alpha \equiv 0$. These M_{tot} and f_{DM} are shown in Fig. 14 while R_{max} can be found in Table 3.

Galaxy (NGC) (1)	β (2)	$M_{tot}(<5\,R_e)$ ($10^{11}\,M_\odot$) (3)	$f_{DM}(<5\,R_e)$ (4)	$M_{tot}(<R_{max})$ ($10^{11}\,M_\odot$) (5)	$f_{DM}(<R_{max})$ (6)
720	0	3.6 ± 0.7	0.46 ± 0.17	13.5 ± 2.2	0.84 ± 0.05
	0.5	3.4 ± 0.7	0.43 ± 0.17	12.7 ± 2.1	0.83 ± 0.04
	−0.5	3.8 ± 0.7	0.48 ± 0.15	13.9 ± 2.3	0.84 ± 0.04
821	0	4.5 ± 0.8	0.82 ± 0.05	7.1 ± 1.2	0.88 ± 0.03
	0.5	4.4 ± 0.8	0.82 ± 0.05	7.0 ± 1.1	0.87 ± 0.03
	−0.5	4.6 ± 0.8	0.82 ± 0.05	7.1 ± 1.2	0.88 ± 0.03
1023	0	1.8 ± 0.3	0.52 ± 0.12	5.2 ± 0.7	0.82 ± 0.04
	0.5	1.8 ± 0.2	0.51 ± 0.11	5.2 ± 0.7	0.82 ± 0.04
	−0.5	1.8 ± 0.3	0.52 ± 0.12	5.3 ± 0.7	0.82 ± 0.04
1400	0	2.4 ± 0.6	0.51 ± 0.28	8.7 ± 1.5	0.85 ± 0.04
	0.5	2.3 ± 0.5	0.49 ± 0.18	8.4 ± 1.5	0.84 ± 0.04
	−0.5	2.4 ± 0.6	0.51 ± 0.18	8.9 ± 1.5	0.85 ± 0.04
1407	0	11.5 ± 1.1	0.71 ± 0.07	35.4 ± 2.7	0.89 ± 0.02
	0.5	10.3 ± 1.0	0.67 ± 0.07	31.8 ± 2.4	0.88 ± 0.02
	−0.5	12.0 ± 1.1	0.72 ± 0.06	37.2 ± 2.8	0.9 ± 0.02
2768	0	7.6 ± 1.1	0.78 ± 0.07	15.9 ± 2.1	0.89 ± 0.03
	0.5	7.2 ± 1.0	0.77 ± 0.07	15.1 ± 2.0	0.88 ± 0.03
	−0.5	7.8 ± 1.1	0.79 ± 0.06	16.3 ± 2.2	0.89 ± 0.03
3115	0	2.0 ± 0.3	0.56 ± 0.08	6.5 ± 0.7	0.86 ± 0.02
	0.5	2.0 ± 0.3	0.56 ± 0.08	6.4 ± 0.7	0.85 ± 0.02
	−0.5	2.0 ± 0.3	0.57 ± 0.08	6.6 ± 0.7	0.86 ± 0.02
3377	0	0.8 ± 0.1	0.67 ± 0.07	2.0 ± 0.3	0.86 ± 0.02
	0.5	0.8 ± 0.1	0.68 ± 0.07	2.1 ± 0.3	0.87 ± 0.02
	−0.5	0.8 ± 0.1	0.67 ± 0.07	2.0 ± 0.3	0.86 ± 0.02
3608	0	3.4 ± 1.1	0.83 ± 0.45	5.3 ± 1.5	0.88 ± 0.06
	0.5	3.4 ± 1.2	0.83 ± 0.56	5.3 ± 1.4	0.88 ± 0.05
	−0.5	3.4 ± 1.1	0.83 ± 0.64	5.3 ± 1.5	0.88 ± 0.12
4278	0	2.9 ± 0.4	0.76 ± 0.06	7.9 ± 0.7	0.9 ± 0.02
	0.5	2.9 ± 0.4	0.76 ± 0.06	7.8 ± 0.7	0.9 ± 0.02
	−0.5	2.9 ± 0.4	0.76 ± 0.06	7.9 ± 0.7	0.9 ± 0.02
4365	0	12.1 ± 1.3	0.78 ± 0.05	29.7 ± 2.5	0.9 ± 0.02
	0.5	11.1 ± 1.2	0.76 ± 0.05	27.3 ± 2.4	0.89 ± 0.02
	−0.5	12.6 ± 1.4	0.79 ± 0.05	31.0 ± 2.6	0.91 ± 0.02
4374	0	14.1 ± 3.3	0.82 ± 0.06	22.7 ± 5.1	0.88 ± 0.03
	0.5	13.1 ± 3.2	0.81 ± 0.07	21.1 ± 4.5	0.87 ± 0.04
	−0.5	14.6 ± 3.5	0.83 ± 0.07	23.6 ± 5.2	0.88 ± 0.04
4473	0	1.5 ± 0.3	0.55 ± 0.13	4.5 ± 0.6	0.84 ± 0.03
	0.5	1.5 ± 0.3	0.55 ± 0.14	4.5 ± 0.6	0.84 ± 0.03
	−0.5	1.5 ± 0.3	0.55 ± 0.12	4.6 ± 0.6	0.84 ± 0.03
4486	0	24.1 ± 1.7	0.88 ± 0.01	141.0 ± 8.2	0.98 ± 0.0
	0.5	22.0 ± 1.6	0.87 ± 0.01	128.0 ± 6.9	0.97 ± 0.0
	−0.5	25.2 ± 1.8	0.88 ± 0.01	148.0 ± 8.2	0.98 ± 0.0
4494	0	1.7 ± 0.3	0.45 ± 0.11	2.5 ± 0.4	0.6 ± 0.08
	0.5	1.7 ± 0.2	0.44 ± 0.11	2.4 ± 0.4	0.59 ± 0.08
	−0.5	1.7 ± 0.2	0.46 ± 0.11	2.5 ± 0.3	0.6 ± 0.08
4526	0	3.5 ± 0.6	0.57 ± 0.12	7.9 ± 1.2	0.79 ± 0.05
	0.5	3.4 ± 0.6	0.55 ± 0.13	7.5 ± 1.1	0.78 ± 0.06
	−0.5	3.6 ± 0.6	0.58 ± 0.13	8.1 ± 1.2	0.79 ± 0.05
4564	0	1.3 ± 0.3	0.73 ± 0.1	1.8 ± 0.4	0.79 ± 0.07
	0.5	1.3 ± 0.3	0.74 ± 0.1	1.8 ± 0.4	0.79 ± 0.07
	−0.5	1.3 ± 0.3	0.73 ± 0.15	1.7 ± 0.4	0.79 ± 0.07
4649	0	11.2 ± 0.9	0.72 ± 0.05	52.7 ± 3.5	0.93 ± 0.01
	0.5	10.2 ± 0.8	0.69 ± 0.06	48.0 ± 3.2	0.93 ± 0.01
	−0.5	11.7 ± 1.0	0.73 ± 0.05	55.1 ± 3.5	0.94 ± 0.01
4697	0	9.4 ± 2.5	0.9 ± 0.05	–	–
	0.5	9.2 ± 2.4	0.9 ± 0.04	–	–
	−0.5	9.5 ± 2.4	0.9 ± 0.04	–	–
5846	0	12.4 ± 1.6	0.83 ± 0.05	33.4 ± 3.6	0.93 ± 0.02
	0.5	11.5 ± 1.5	0.81 ± 0.05	31.0 ± 3.4	0.92 ± 0.02
	−0.5	12.8 ± 1.7	0.83 ± 0.04	34.6 ± 3.7	0.93 ± 0.02
7457	0	1.7 ± 0.4	0.89 ± 0.04	1.8 ± 0.4	0.9 ± 0.04
	0.5	1.7 ± 0.4	0.9 ± 0.04	1.9 ± 0.4	0.91 ± 0.04
	−0.5	1.6 ± 0.4	0.89 ± 0.04	1.8 ± 0.4	0.9 ± 0.04
3607	0	2.6 ± 0.7	0.33 ± 0.34	11.1 ± 2.7	0.82 ± 0.06
	0.5	2.5 ± 0.7	0.3 ± 0.44	10.5 ± 2.5	0.81 ± 0.13
	−0.5	2.7 ± 0.7	0.35 ± 0.28	11.4 ± 2.8	0.83 ± 0.07
5866	0	1.6 ± 0.6	0.46 ± 0.45	–	–
	0.5	1.5 ± 0.6	0.44 ± 0.45	–	–
	−0.5	1.6 ± 0.6	0.46 ± 0.45	–	–

Table A3. Mass estimates ($M_{\rm tot}$) and DM fractions ($f_{\rm DM}$) within $5\,R_{\rm e}$ and $R_{\rm max}$ assuming different anisotropy, obtained with stellar M/L corresponding to a Salpeter IMF from Cappellari et al. (2013a,b) (see Section 3.8 for details). Columns 3–6 show $M_{\rm tot}$ and $f_{\rm DM}$ obtained by allowing α to vary while in columns 7–10, $\alpha \equiv 0$, $R_{\rm max}$ can be found in Table 3.

Galaxy (NGC)	β	$M_{\rm tot}(<5\,R_{\rm e})$ $(10^{11}\,{\rm M}_{\odot})$	$f_{\rm DM}(<5\,R_{\rm e})$	$M_{\rm tot}(<R_{\rm max})$ $(10^{11}\,{\rm M}_{\odot})$	$f_{\rm DM}(<R_{\rm max})$	$M_{\rm tot}(<5\,R_{\rm e})$ $(10^{11}\,{\rm M}_{\odot})$	$f_{\rm DM}(<5\,R_{\rm e})$	$M_{\rm tot}(<R_{\rm max})$ $(10^{11}\,{\rm M}_{\odot})$	$f_{\rm DM}(<R_{\rm max})$
(1)	(2)	(3)	(4)	(5)	(6)	(7)	(8)	(9)	(10)
720	0	3.6 ± 0.7	0.28 ± 0.41	13.5 ± 2.3	0.78 ± 0.11	3.6 ± 0.7	0.28 ± 0.41	13.5 ± 2.4	0.78 ± 0.11
	0.5	3.4 ± 0.7	0.23 ± 0.43	12.7 ± 2.2	0.77 ± 0.12	3.4 ± 0.7	0.23 ± 0.42	12.7 ± 2.1	0.77 ± 0.11
	−0.5	3.8 ± 0.7	0.3 ± 0.39	13.9 ± 2.4	0.79 ± 0.11	3.8 ± 0.8	0.3 ± 0.4	13.9 ± 2.4	0.79 ± 0.1
821	0	4.3 ± 0.8	0.77 ± 0.06	6.1 ± 1.0	0.83 ± 0.04	4.5 ± 0.8	0.78 ± 0.06	7.1 ± 1.2	0.85 ± 0.03
	0.5	4.4 ± 0.8	0.78 ± 0.06	6.3 ± 1.1	0.83 ± 0.04	4.4 ± 0.8	0.78 ± 0.06	7.0 ± 1.2	0.85 ± 0.04
	−0.5	4.2 ± 0.8	0.77 ± 0.05	6.0 ± 1.0	0.83 ± 0.04	4.6 ± 0.8	0.79 ± 0.05	7.1 ± 1.2	0.85 ± 0.04
1023	0	1.7 ± 0.2	0.29 ± 0.15	4.2 ± 0.5	0.7 ± 0.05	1.8 ± 0.3	0.34 ± 0.14	5.2 ± 0.7	0.75 ± 0.05
	0.5	1.7 ± 0.3	0.31 ± 0.15	4.3 ± 0.6	0.7 ± 0.05	1.7 ± 0.3	0.33 ± 0.14	5.1 ± 0.7	0.75 ± 0.05
	−0.5	1.7 ± 0.2	0.29 ± 0.15	4.2 ± 0.5	0.69 ± 0.06	1.8 ± 0.3	0.34 ± 0.13	5.3 ± 0.7	0.75 ± 0.05
1400	0	2.4 ± 0.6	0.36 ± 0.41	7.7 ± 1.4	0.78 ± 0.11	2.4 ± 0.5	0.37 ± 0.42	8.7 ± 1.5	0.81 ± 0.1
	0.5	2.3 ± 0.6	0.36 ± 0.42	7.7 ± 1.3	0.78 ± 0.11	2.3 ± 0.5	0.34 ± 0.38	8.4 ± 1.5	0.8 ± 0.1
	−0.5	2.4 ± 0.6	0.36 ± 0.43	7.8 ± 1.4	0.78 ± 0.11	2.4 ± 0.6	0.38 ± 0.41	8.9 ± 1.6	0.81 ± 0.09
1407	0	11.6 ± 1.1	0.58 ± 0.21	38.2 ± 2.9	0.86 ± 0.07	11.5 ± 1.1	0.58 ± 0.22	35.4 ± 2.5	0.84 ± 0.06
	0.5	10.0 ± 1.0	0.51 ± 0.25	32.8 ± 2.3	0.83 ± 0.07	10.3 ± 1.0	0.53 ± 0.24	31.8 ± 2.4	0.83 ± 0.08
	−0.5	12.4 ± 1.3	0.61 ± 0.2	41.0 ± 3.1	0.87 ± 0.06	12.0 ± 1.2	0.59 ± 0.22	37.2 ± 2.7	0.85 ± 0.06
2768	0	7.4 ± 1.0	0.72 ± 0.06	15.0 ± 2.0	0.85 ± 0.03	7.6 ± 1.1	0.73 ± 0.06	16.0 ± 2.1	0.86 ± 0.03
	0.5	7.1 ± 0.9	0.71 ± 0.06	14.5 ± 1.8	0.84 ± 0.03	7.2 ± 0.9	0.72 ± 0.06	15.2 ± 2.1	0.85 ± 0.03
	−0.5	7.5 ± 1.0	0.73 ± 0.05	15.3 ± 2.0	0.85 ± 0.03	7.8 ± 1.1	0.74 ± 0.06	16.4 ± 2.1	0.86 ± 0.03
3115	0	2.0 ± 0.3	0.47 ± 0.26	5.8 ± 0.6	0.8 ± 0.09	2.0 ± 0.3	0.47 ± 0.26	6.5 ± 0.7	0.82 ± 0.08
	0.5	2.1 ± 0.3	0.48 ± 0.25	5.9 ± 0.6	0.81 ± 0.08	2.0 ± 0.3	0.46 ± 0.25	6.4 ± 0.7	0.82 ± 0.08
	−0.5	2.0 ± 0.3	0.46 ± 0.26	5.7 ± 0.6	0.8 ± 0.09	2.0 ± 0.3	0.47 ± 0.26	6.6 ± 0.7	0.83 ± 0.08
3377	0	0.6 ± 0.1	0.37 ± 0.14	1.3 ± 0.2	0.69 ± 0.06	0.8 ± 0.1	0.49 ± 0.12	2.0 ± 0.3	0.79 ± 0.04
	0.5	0.7 ± 0.1	0.43 ± 0.12	1.5 ± 0.2	0.72 ± 0.05	0.8 ± 0.1	0.5 ± 0.11	2.0 ± 0.3	0.79 ± 0.04
	−0.5	0.6 ± 0.1	0.34 ± 0.16	1.3 ± 0.2	0.67 ± 0.06	0.7 ± 0.1	0.49 ± 0.11	1.9 ± 0.3	0.79 ± 0.04
3608	0	3.3 ± 1.0	0.66 ± 0.24	4.6 ± 1.2	0.74 ± 0.11	3.3 ± 1.1	0.66 ± 0.93	5.1 ± 1.3	0.76 ± 0.11
	0.5	3.4 ± 1.1	0.67 ± 0.42	4.7 ± 1.3	0.74 ± 0.1	3.2 ± 1.0	0.66 ± 0.45	5.0 ± 1.4	0.76 ± 0.12
	−0.5	3.2 ± 1.0	0.66 ± 0.26	4.5 ± 1.3	0.74 ± 0.12	3.3 ± 1.1	0.67 ± 0.23	5.1 ± 1.4	0.77 ± 0.18
4278	0	2.8 ± 0.3	0.59 ± 0.08	6.8 ± 0.6	0.82 ± 0.03	2.8 ± 0.3	0.6 ± 0.07	7.7 ± 0.7	0.84 ± 0.02
	0.5	2.8 ± 0.3	0.6 ± 0.07	7.0 ± 0.6	0.82 ± 0.03	2.8 ± 0.3	0.59 ± 0.07	7.5 ± 0.7	0.84 ± 0.02
	−0.5	2.7 ± 0.3	0.59 ± 0.08	6.7 ± 0.6	0.82 ± 0.03	2.9 ± 0.4	0.61 ± 0.07	7.8 ± 0.7	0.84 ± 0.02
4365	0	12.3 ± 1.3	0.69 ± 0.05	31.8 ± 2.9	0.87 ± 0.02	12.0 ± 1.2	0.68 ± 0.06	29.6 ± 2.6	0.86 ± 0.02
	0.5	11.0 ± 1.2	0.65 ± 0.06	28.3 ± 2.6	0.85 ± 0.02	11.0 ± 1.2	0.65 ± 0.06	27.1 ± 2.4	0.84 ± 0.02
	−0.5	13.0 ± 1.4	0.7 ± 0.05	33.6 ± 3.0	0.87 ± 0.02	12.5 ± 1.4	0.69 ± 0.05	30.9 ± 2.7	0.86 ± 0.02
4374	0	14.2 ± 3.5	0.75 ± 0.12	23.7 ± 5.0	0.84 ± 0.05	14.0 ± 3.3	0.74 ± 0.09	22.7 ± 4.9	0.83 ± 0.05
	0.5	12.9 ± 3.1	0.72 ± 0.09	21.5 ± 4.7	0.82 ± 0.05	13.0 ± 3.2	0.72 ± 0.12	20.9 ± 4.4	0.81 ± 0.06
	−0.5	14.9 ± 3.6	0.76 ± 0.08	24.8 ± 5.5	0.84 ± 0.05	14.6 ± 3.5	0.75 ± 0.1	23.5 ± 4.8	0.83 ± 0.05
4473	0	1.4 ± 0.3	0.37 ± 0.17	3.8 ± 0.5	0.74 ± 0.05	1.5 ± 0.3	0.39 ± 0.16	4.5 ± 0.6	0.78 ± 0.04
	0.5	1.5 ± 0.3	0.39 ± 0.15	3.9 ± 0.6	0.75 ± 0.05	1.5 ± 0.3	0.39 ± 0.16	4.5 ± 0.6	0.78 ± 0.04
	−0.5	1.4 ± 0.3	0.35 ± 0.19	3.7 ± 0.5	0.73 ± 0.05	1.5 ± 0.3	0.4 ± 0.16	4.5 ± 0.6	0.78 ± 0.04
4486	0	23.9 ± 1.7	0.8 ± 0.03	166.0 ± 9.0	0.97 ± 0.0	23.8 ± 1.7	0.79 ± 0.03	139.0 ± 7.8	0.96 ± 0.01
	0.5	20.6 ± 1.5	0.76 ± 0.04	143.0 ± 8.3	0.96 ± 0.01	21.4 ± 1.5	0.77 ± 0.03	125.0 ± 7.0	0.96 ± 0.01
	−0.5	25.6 ± 1.8	0.81 ± 0.03	178.0 ± 10.0	0.97 ± 0.0	24.9 ± 1.8	0.8 ± 0.03	146.0 ± 8.3	0.96 ± 0.0
4494	0	1.5 ± 0.2	0.29 ± 0.14	2.2 ± 0.3	0.46 ± 0.11	1.7 ± 0.3	0.36 ± 0.15	2.5 ± 0.4	0.53 ± 0.09
	0.5	1.6 ± 0.2	0.31 ± 0.14	2.2 ± 0.3	0.47 ± 0.11	1.7 ± 0.2	0.34 ± 0.14	2.4 ± 0.3	0.52 ± 0.1
	−0.5	1.5 ± 0.2	0.29 ± 0.15	2.2 ± 0.3	0.45 ± 0.11	1.7 ± 0.3	0.36 ± 0.14	2.5 ± 0.4	0.53 ± 0.09
4526	0	3.5 ± 0.6	0.53 ± 0.11	7.4 ± 1.1	0.76 ± 0.05	3.6 ± 0.7	0.54 ± 0.11	8.0 ± 1.2	0.77 ± 0.05
	0.5	3.5 ± 0.6	0.52 ± 0.11	7.3 ± 1.1	0.75 ± 0.05	3.5 ± 0.6	0.52 ± 0.12	7.7 ± 1.2	0.76 ± 0.05
	−0.5	3.5 ± 0.6	0.53 ± 0.11	7.5 ± 1.1	0.76 ± 0.05	3.7 ± 0.6	0.55 ± 0.11	8.1 ± 1.2	0.78 ± 0.05
4564	0	1.1 ± 0.2	0.56 ± 0.16	1.3 ± 0.3	0.64 ± 0.1	1.3 ± 0.3	0.65 ± 0.13	1.7 ± 0.4	0.72 ± 0.09
	0.5	1.1 ± 0.3	0.59 ± 0.14	1.4 ± 0.3	0.66 ± 0.11	1.3 ± 0.3	0.65 ± 0.12	1.8 ± 0.4	0.73 ± 0.09
	−0.5	1.0 ± 0.2	0.55 ± 0.15	1.3 ± 0.3	0.63 ± 0.1	1.3 ± 0.3	0.65 ± 0.13	1.7 ± 0.4	0.72 ± 0.08
4649	0	11.5 ± 0.9	0.57 ± 0.07	63.1 ± 4.4	0.91 ± 0.01	11.1 ± 0.9	0.56 ± 0.07	52.1 ± 3.5	0.89 ± 0.01
	0.5	9.9 ± 0.8	0.5 ± 0.08	54.4 ± 3.7	0.9 ± 0.01	10.0 ± 0.8	0.51 ± 0.08	47.1 ± 3.2	0.88 ± 0.02
	−0.5	12.3 ± 1.0	0.6 ± 0.06	67.5 ± 4.7	0.92 ± 0.01	11.6 ± 0.9	0.57 ± 0.07	54.6 ± 3.7	0.9 ± 0.01
4697	0	9.1 ± 2.4	0.86 ± 0.07	–	–	9.3 ± 2.4	0.86 ± 0.05	–	–
	0.5	9.2 ± 2.4	0.86 ± 0.06	–	–	9.1 ± 2.3	0.86 ± 0.06	–	–
	−0.5	9.1 ± 2.3	0.86 ± 0.05	–	–	9.4 ± 2.6	0.86 ± 0.06	–	–
5846	0	12.4 ± 1.6	0.77 ± 0.04	34.0 ± 3.6	0.91 ± 0.02	12.4 ± 1.7	0.77 ± 0.04	33.6 ± 3.6	0.91 ± 0.02
	0.5	11.5 ± 1.5	0.75 ± 0.05	31.4 ± 3.3	0.9 ± 0.02	11.6 ± 1.5	0.76 ± 0.05	31.2 ± 3.3	0.9 ± 0.02
	−0.5	12.9 ± 1.7	0.78 ± 0.04	35.3 ± 3.8	0.91 ± 0.01	12.9 ± 1.7	0.78 ± 0.04	34.7 ± 3.7	0.91 ± 0.02

Table A3 – *continued.*

Galaxy (NGC)	β	$M_{\rm tot}(<5\,R_{\rm e})$ ($10^{11}\,{\rm M}_\odot$)	$f_{\rm DM}(<5\,R_{\rm e})$	$M_{\rm tot}(<R_{\rm max})$ ($10^{11}\,{\rm M}_\odot$)	$f_{\rm DM}(<R_{\rm max})$	$M_{\rm tot}(<5\,R_{\rm e})$ ($10^{11}\,{\rm M}_\odot$)	$f_{\rm DM}(<5\,R_{\rm e})$	$M_{\rm tot}(<R_{\rm max})$ ($10^{11}\,{\rm M}_\odot$)	$f_{\rm DM}(<R_{\rm max})$
(1)	(2)	(3)	(4)	(5)	(6)	(7)	(8)	(9)	(10)
7457	0	1.1 ± 0.2	0.87 ± 0.04	1.2 ± 0.2	0.88 ± 0.04	1.7 ± 0.4	0.92 ± 0.03	1.9 ± 0.4	0.92 ± 0.02
	0.5	1.3 ± 0.3	0.89 ± 0.04	1.3 ± 0.3	0.89 ± 0.03	1.8 ± 0.4	0.92 ± 0.03	1.9 ± 0.4	0.92 ± 0.02
	−0.5	1.0 ± 0.2	0.86 ± 0.04	1.1 ± 0.2	0.87 ± 0.04	1.6 ± 0.4	0.91 ± 0.03	1.8 ± 0.4	0.92 ± 0.03
3607	0	2.6 ± 0.7	0.01 ± 0.45	10.9 ± 2.6	0.74 ± 0.1	2.6 ± 0.7	0.01 ± 0.45	11.0 ± 2.7	0.74 ± 0.09
	0.5	2.4 ± 0.6	-0.0 ± 0.45	10.3 ± 2.4	0.72 ± 0.09	2.4 ± 0.6	-0.0 ± 0.45	10.3 ± 2.5	0.72 ± 0.09
	−0.5	2.6 ± 0.7	0.04 ± 0.41	11.2 ± 2.7	0.75 ± 0.09	2.7 ± 0.7	0.04 ± 0.45	11.4 ± 2.7	0.75 ± 0.08
5866	0	1.3 ± 0.5	0.33 ± 0.45	–	–	1.6 ± 0.6	0.46 ± 0.45	–	–
	0.5	1.3 ± 0.5	0.36 ± 0.45	–	–	1.6 ± 0.6	0.46 ± 0.45	–	–
	−0.5	1.2 ± 0.5	0.32 ± 0.45	–	–	1.6 ± 0.6	0.46 ± 0.45	–	–

Table A4. Mass estimates ($M_{\rm tot}$) and DM fractions ($f_{\rm DM}$) within $5\,R_{\rm e}$ and $R_{\rm max}$ assuming different anisotropy, obtained using the best-fitting stellar M/L ratios from the dynamical modelling of Cappellari et al. (2013a,b), i.e. total dynamical mass minus DM mass (see Section 3.8 for details). Columns 3–6 show $M_{\rm tot}$ and $f_{\rm DM}$ obtained by allowing α to vary, while in columns 7–10, $\alpha \equiv 0$, $R_{\rm max}$ can be found in Table 3.

Galaxy (NGC)	β	$M_{\rm tot}(<5\,R_{\rm e})$ ($10^{11}\,{\rm M}_\odot$)	$f_{\rm DM}(<5\,R_{\rm e})$	$M_{\rm tot}(<R_{\rm max})$ ($10^{11}\,{\rm M}_\odot$)	$f_{\rm DM}(<R_{\rm max})$	$M_{\rm tot}(<5\,R_{\rm e})$ ($10^{11}\,{\rm M}_\odot$)	$f_{\rm DM}(<5\,R_{\rm e})$	$M_{\rm tot}(<R_{\rm max})$ ($10^{11}\,{\rm M}_\odot$)	$f_{\rm DM}(<R_{\rm max})$
(1)	(2)	(3)	(4)	(5)	(6)	(7)	(8)	(9)	(10)
720	0	3.5 ± 0.7	0.46 ± 0.13	11.5 ± 2.0	0.81 ± 0.04	3.6 ± 0.7	0.46 ± 0.14	13.2 ± 2.3	0.84 ± 0.04
	0.5	3.4 ± 0.7	0.44 ± 0.15	11.1 ± 1.8	0.8 ± 0.04	3.3 ± 0.7	0.42 ± 0.15	12.3 ± 2.2	0.82 ± 0.04
	−0.5	3.6 ± 0.7	0.47 ± 0.14	11.7 ± 2.0	0.81 ± 0.04	3.7 ± 0.7	0.48 ± 0.14	13.7 ± 2.3	0.84 ± 0.04
821	0	4.1 ± 0.8	0.78 ± 0.06	5.7 ± 0.9	0.83 ± 0.04	4.4 ± 0.8	0.8 ± 0.05	7.0 ± 1.2	0.86 ± 0.03
	0.5	4.3 ± 0.8	0.79 ± 0.06	5.9 ± 1.0	0.84 ± 0.04	4.3 ± 0.8	0.79 ± 0.05	6.8 ± 1.1	0.86 ± 0.03
	−0.5	4.0 ± 0.8	0.78 ± 0.06	5.6 ± 0.9	0.83 ± 0.04	4.5 ± 0.8	0.8 ± 0.05	7.1 ± 1.2	0.86 ± 0.03
1023	0	1.6 ± 0.2	0.63 ± 0.08	3.5 ± 0.4	0.81 ± 0.03	1.9 ± 0.3	0.68 ± 0.07	5.4 ± 0.7	0.88 ± 0.02
	0.5	1.7 ± 0.3	0.65 ± 0.08	3.7 ± 0.5	0.82 ± 0.03	1.8 ± 0.3	0.68 ± 0.07	5.4 ± 0.7	0.88 ± 0.02
	−0.5	1.5 ± 0.2	0.61 ± 0.08	3.4 ± 0.4	0.81 ± 0.03	1.9 ± 0.3	0.68 ± 0.07	5.4 ± 0.7	0.88 ± 0.02
1400	0	2.3 ± 0.5	0.46 ± 0.18	6.9 ± 1.2	0.8 ± 0.05	2.4 ± 0.5	0.47 ± 0.16	8.6 ± 1.5	0.84 ± 0.04
	0.5	2.3 ± 0.5	0.46 ± 0.37	6.9 ± 1.2	0.8 ± 0.05	2.2 ± 0.5	0.45 ± 0.17	8.2 ± 1.4	0.83 ± 0.04
	−0.5	2.3 ± 0.5	0.46 ± 0.18	6.8 ± 1.3	0.8 ± 0.05	2.4 ± 0.6	0.48 ± 0.18	8.7 ± 1.6	0.84 ± 0.04
1407	0	10.8 ± 1.1	0.61 ± 0.06	33.9 ± 2.5	0.86 ± 0.02	10.8 ± 1.0	0.61 ± 0.06	33.3 ± 2.4	0.86 ± 0.02
	0.5	9.2 ± 0.9	0.55 ± 0.06	28.9 ± 2.2	0.84 ± 0.02	9.3 ± 0.9	0.55 ± 0.07	28.7 ± 2.1	0.84 ± 0.02
	−0.5	11.6 ± 1.1	0.64 ± 0.05	36.4 ± 2.8	0.87 ± 0.01	11.5 ± 1.2	0.64 ± 0.05	35.6 ± 2.6	0.87 ± 0.02
2768	0	6.8 ± 0.9	0.57 ± 0.09	13.9 ± 1.8	0.77 ± 0.04	6.9 ± 1.0	0.58 ± 0.09	14.6 ± 1.8	0.78 ± 0.04
	0.5	6.2 ± 0.8	0.52 ± 0.1	12.6 ± 1.7	0.74 ± 0.05	6.2 ± 0.8	0.53 ± 0.1	13.1 ± 1.7	0.75 ± 0.05
	−0.5	7.1 ± 1.0	0.58 ± 0.08	14.5 ± 1.9	0.77 ± 0.04	7.3 ± 1.0	0.6 ± 0.08	15.3 ± 2.0	0.79 ± 0.04
3115	0	2.0 ± 0.3	0.57 ± 0.08	5.4 ± 0.6	0.83 ± 0.02	2.0 ± 0.3	0.57 ± 0.08	6.5 ± 0.7	0.86 ± 0.02
	0.5	2.1 ± 0.3	0.59 ± 0.07	5.6 ± 0.6	0.83 ± 0.02	2.0 ± 0.3	0.56 ± 0.08	6.4 ± 0.7	0.85 ± 0.02
	−0.5	2.0 ± 0.3	0.56 ± 0.08	5.3 ± 0.6	0.82 ± 0.02	2.0 ± 0.3	0.57 ± 0.08	6.6 ± 0.7	0.86 ± 0.02
3377	0	0.6 ± 0.1	0.57 ± 0.1	1.2 ± 0.2	0.78 ± 0.04	0.8 ± 0.1	0.68 ± 0.07	2.0 ± 0.3	0.87 ± 0.03
	0.5	0.7 ± 0.1	0.62 ± 0.09	1.4 ± 0.2	0.81 ± 0.04	0.8 ± 0.1	0.69 ± 0.07	2.1 ± 0.3	0.87 ± 0.02
	−0.5	0.5 ± 0.1	0.54 ± 0.1	1.2 ± 0.2	0.76 ± 0.05	0.8 ± 0.1	0.67 ± 0.07	2.0 ± 0.3	0.86 ± 0.03
3608	0	3.3 ± 1.1	0.78 ± 0.25	4.3 ± 1.2	0.81 ± 0.37	3.3 ± 1.1	0.78 ± 2.63	5.1 ± 1.4	0.85 ± 0.18
	0.5	3.5 ± 1.0	0.79 ± 0.14	4.5 ± 1.3	0.82 ± 0.22	3.3 ± 1.0	0.78 ± 0.13	5.1 ± 1.4	0.84 ± 0.08
	−0.5	3.2 ± 1.1	0.77 ± 0.25	4.1 ± 1.1	0.81 ± 0.09	3.4 ± 1.1	0.78 ± 0.31	5.2 ± 1.4	0.85 ± 0.82
4278	0	2.7 ± 0.3	0.68 ± 0.06	6.3 ± 0.5	0.85 ± 0.02	2.8 ± 0.3	0.69 ± 0.06	7.7 ± 0.7	0.88 ± 0.02
	0.5	2.9 ± 0.3	0.69 ± 0.06	6.6 ± 0.6	0.86 ± 0.02	2.8 ± 0.4	0.69 ± 0.06	7.5 ± 0.7	0.87 ± 0.02
	−0.5	2.6 ± 0.3	0.67 ± 0.06	6.1 ± 0.6	0.85 ± 0.02	2.9 ± 0.3	0.7 ± 0.05	7.8 ± 0.7	0.88 ± 0.02
4365	0	11.6 ± 1.2	0.78 ± 0.04	27.4 ± 2.5	0.9 ± 0.02	11.8 ± 1.2	0.78 ± 0.04	29.1 ± 2.6	0.9 ± 0.02
	0.5	10.7 ± 1.1	0.76 ± 0.04	25.3 ± 2.3	0.89 ± 0.02	10.6 ± 1.1	0.76 ± 0.04	26.2 ± 2.3	0.89 ± 0.02
	−0.5	12.0 ± 1.2	0.79 ± 0.04	28.5 ± 2.5	0.9 ± 0.01	12.4 ± 1.3	0.79 ± 0.04	30.5 ± 2.8	0.91 ± 0.01
4374	0	13.4 ± 3.2	0.78 ± 0.07	21.1 ± 4.5	0.85 ± 0.05	13.5 ± 3.3	0.78 ± 0.09	21.7 ± 4.8	0.85 ± 0.05
	0.5	12.2 ± 2.9	0.76 ± 0.08	19.3 ± 4.2	0.83 ± 0.05	12.1 ± 2.9	0.75 ± 0.09	19.6 ± 4.2	0.84 ± 0.05
	−0.5	14.0 ± 3.2	0.79 ± 0.13	22.1 ± 4.7	0.85 ± 0.04	14.2 ± 3.4	0.79 ± 0.07	22.8 ± 5.0	0.86 ± 0.05
4473	0	1.4 ± 0.3	0.6 ± 0.11	3.4 ± 0.5	0.82 ± 0.03	1.5 ± 0.3	0.63 ± 0.19	4.6 ± 0.6	0.87 ± 0.02
	0.5	1.5 ± 0.3	0.64 ± 0.09	3.7 ± 0.5	0.84 ± 0.03	1.5 ± 0.3	0.63 ± 0.11	4.6 ± 0.6	0.87 ± 0.03
	−0.5	1.4 ± 0.3	0.59 ± 0.12	3.3 ± 0.5	0.81 ± 0.04	1.5 ± 0.3	0.63 ± 0.11	4.6 ± 0.6	0.87 ± 0.03
4486	0	22.4 ± 1.6	0.81 ± 0.03	136.0 ± 7.6	0.96 ± 0.0	22.4 ± 1.7	0.81 ± 0.03	131.0 ± 7.4	0.96 ± 0.0
	0.5	19.1 ± 1.3	0.78 ± 0.04	116.0 ± 6.8	0.96 ± 0.01	19.4 ± 1.4	0.78 ± 0.03	113.0 ± 6.5	0.96 ± 0.01
	−0.5	24.1 ± 1.7	0.83 ± 0.03	146.0 ± 8.3	0.97 ± 0.0	23.9 ± 1.7	0.83 ± 0.03	140.0 ± 8.0	0.97 ± 0.0

Table A4 – *continued*.

Galaxy (NGC) (1)	β (2)	$M_{\rm tot}(<5\,R_{\rm e})$ ($10^{11}\,{\rm M}_{\odot}$) (3)	$f_{\rm DM}(<5\,R_{\rm e})$ (4)	$M_{\rm tot}(<R_{\rm max})$ ($10^{11}\,{\rm M}_{\odot}$) (5)	$f_{\rm DM}(<R_{\rm max})$ (6)	$M_{\rm tot}(<5\,R_{\rm e})$ ($10^{11}\,{\rm M}_{\odot}$) (7)	$f_{\rm DM}(<5\,R_{\rm e})$ (8)	$M_{\rm tot}(<R_{\rm max})$ ($10^{11}\,{\rm M}_{\odot}$) (9)	$f_{\rm DM}(<R_{\rm max})$ (10)
4494	0	1.5 ± 0.2	0.51 ± 0.11	2.0 ± 0.3	0.61 ± 0.07	1.7 ± 0.2	0.59 ± 0.08	2.5 ± 0.4	0.7 ± 0.06
	0.5	1.5 ± 0.2	0.54 ± 0.1	2.1 ± 0.3	0.63 ± 0.07	1.7 ± 0.2	0.58 ± 0.08	2.5 ± 0.4	0.7 ± 0.06
	−0.5	1.4 ± 0.2	0.5 ± 0.11	1.9 ± 0.3	0.6 ± 0.08	1.7 ± 0.2	0.59 ± 0.08	2.6 ± 0.4	0.7 ± 0.06
4526	0	3.3 ± 0.6	0.53 ± 0.11	6.8 ± 1.0	0.75 ± 0.05	3.5 ± 0.6	0.55 ± 0.11	7.7 ± 1.1	0.78 ± 0.04
	0.5	3.3 ± 0.6	0.53 ± 0.12	6.7 ± 1.0	0.75 ± 0.05	3.3 ± 0.6	0.53 ± 0.11	7.3 ± 1.1	0.77 ± 0.05
	−0.5	3.4 ± 0.6	0.54 ± 0.12	6.9 ± 1.0	0.75 ± 0.05	3.6 ± 0.6	0.57 ± 0.11	7.9 ± 1.2	0.79 ± 0.05
4564	0	1.0 ± 0.2	0.65 ± 0.11	1.3 ± 0.3	0.71 ± 0.08	1.3 ± 0.3	0.74 ± 0.09	1.8 ± 0.4	0.8 ± 0.07
	0.5	1.1 ± 0.3	0.68 ± 0.12	1.4 ± 0.3	0.73 ± 0.07	1.4 ± 0.3	0.75 ± 0.09	1.8 ± 0.4	0.8 ± 0.06
	−0.5	0.9 ± 0.2	0.63 ± 0.11	1.2 ± 0.2	0.7 ± 0.08	1.3 ± 0.3	0.74 ± 0.11	1.8 ± 0.4	0.79 ± 0.07
4649	0	10.6 ± 0.8	0.63 ± 0.05	50.9 ± 3.5	0.91 ± 0.01	10.5 ± 0.8	0.62 ± 0.06	49.6 ± 3.2	0.91 ± 0.01
	0.5	9.2 ± 0.7	0.57 ± 0.07	44.2 ± 2.9	0.9 ± 0.01	9.2 ± 0.7	0.57 ± 0.07	43.4 ± 2.9	0.9 ± 0.01
	−0.5	11.3 ± 0.9	0.65 ± 0.06	54.2 ± 3.7	0.92 ± 0.01	11.2 ± 0.9	0.65 ± 0.06	52.8 ± 3.5	0.92 ± 0.01
4697	0	8.9 ± 2.3	0.88 ± 0.26	–	–	9.3 ± 2.3	0.89 ± 0.04	–	–
	0.5	9.1 ± 2.2	0.89 ± 0.04	–	–	9.0 ± 2.2	0.89 ± 0.08	–	–
	−0.5	8.8 ± 2.3	0.88 ± 0.05	–	–	9.4 ± 2.4	0.89 ± 0.05	–	–
5846	0	11.8 ± 1.5	0.76 ± 0.05	30.7 ± 3.3	0.9 ± 0.02	11.7 ± 1.6	0.76 ± 0.05	31.6 ± 3.4	0.9 ± 0.02
	0.5	10.7 ± 1.4	0.74 ± 0.05	28.0 ± 3.1	0.89 ± 0.02	10.5 ± 1.3	0.74 ± 0.05	28.4 ± 3.1	0.89 ± 0.02
	−0.5	12.3 ± 1.7	0.77 ± 0.04	32.1 ± 3.4	0.9 ± 0.02	12.3 ± 1.6	0.77 ± 0.04	33.3 ± 3.5	0.91 ± 0.02
7457	0	1.0 ± 0.2	0.92 ± 0.03	1.1 ± 0.2	0.92 ± 0.02	1.8 ± 0.4	0.95 ± 0.02	2.0 ± 0.4	0.95 ± 0.01
	0.5	1.2 ± 0.3	0.93 ± 0.02	1.3 ± 0.3	0.93 ± 0.02	1.9 ± 0.4	0.95 ± 0.01	2.1 ± 0.5	0.96 ± 0.01
	−0.5	1.0 ± 0.2	0.91 ± 0.03	1.0 ± 0.2	0.91 ± 0.02	1.7 ± 0.4	0.95 ± 0.02	1.9 ± 0.4	0.95 ± 0.02
3607	0	2.4 ± 0.7	0.21 ± 0.45	9.3 ± 2.2	0.78 ± 0.08	2.5 ± 0.7	0.27 ± 0.45	10.8 ± 2.6	0.81 ± 0.08
	0.5	2.3 ± 0.6	0.19 ± 0.45	9.0 ± 2.2	0.77 ± 0.1	2.4 ± 0.6	0.21 ± 0.45	10.1 ± 2.4	0.79 ± 0.07
	−0.5	2.4 ± 0.6	0.23 ± 0.36	9.4 ± 2.2	0.78 ± 0.07	2.6 ± 0.7	0.3 ± 0.28	11.2 ± 2.8	0.81 ± 0.07
5866	0	1.2 ± 0.5	0.24 ± 0.45	–	–	1.5 ± 0.6	0.41 ± 0.45	–	–
	0.5	1.2 ± 0.5	0.27 ± 0.45	–	–	1.5 ± 0.6	0.4 ± 0.45	–	–
	−0.5	1.2 ± 0.5	0.22 ± 0.45	–	–	1.6 ± 0.6	0.42 ± 0.45	–	–

This paper has been typeset from a TEX/LATEX file prepared by the author.